PRESSURE DEPENDENCE OF SPACE CHARGE DEPOSITION IN PIEZOELECTRIC POLYMER FOAMS: SIMULATIONS AND EXPERIMENTAL VERIFICATION

Scott Harris

A thesis submitted in partial fulfillment of
the requirements for the degree of
Master of Science

Department of Physics

Central Michigan University
Mount Pleasant, Michigan
February, 2012

Accepted by the Faculty of the College of Graduate Studies,

Central Michigan University, in partial fulfillment of

the requirements for the master's degree

Thesis Committee:

Committee Chair

Faculty Member

Faculty Member

Date: 2/28/2012

Dean
College of Graduate Studies

Date: 4/5/12

Committee:

Axel Mellinger, Ph.D., Chair

Andrzej Sieradzan, Ph.D.

Stanley Hirschi, Ph.D.

ACKNOWLEDGMENTS

I would like to thank my advisor Dr. Axel Mellinger the guidance and encouragement he has provided during my time at Central Michigan University. I would also like to thank Dr. Hirschi and Dr. Sieradzan for agreeing to be part of my thesis committee and providing feedback on my thesis. Finally, I would like to thank the department of physics at Central Michigan University and the Advanced Materials Research Initiative for providing the funding and opportunity to perform this study.

ABSTRACT

PRESSURE DEPENDENCE OF SPACE CHARGE DEPOSITION IN PIEZOELECTRIC POLYMER FOAMS: SIMULATIONS AND EXPERIMENTAL VERIFICATION

by Scott Harris

The piezoelectric activity of PQ-50 cellular polypropylene (PP) foam (an example of a so-called ferroelectret) is measured after repeated charging in a nitrogen atmosphere at a range of pressures between 61 and 381 kPa. The results are compared against simulations using a multi-layer electromechanical model based on Townsend's model of Paschen breakdown and a realistic distribution of void heights determined from scanning electron micrographs. The modeled piezoelectric coefficients versus pressure are in good agreement with experimental data when adjusted Paschen coefficients are used, indicating that the Paschen curve for electric breakdown in gases needs to be modified for dielectric barrier discharges in micro-cavities. The highest d_{33} coefficients were achieved for pressures above 251 kPa. For previously uncharged PP foam, the model predicts an optimal charging pressure of 186 kPa.

TABLE OF CONTENTS

LIST OF FIGURES....vi

CHAPTER

I. INTRODUCTION....1
1.1 Piezoelectric Properties....2
1.2 Model....3

II. MODELING THE CHARGING PROCESS....5
2.1 Electromechanical Model....5
2.2 Computational Algorithm....10

III. EXPERIMENT....14
3.1 Sample Preparation....14
3.1.1 Sample Inflation....14
3.1.2 Dilatometry....16
3.2 Sample Charging....19
3.3 Measurement of Piezoelectric Coefficient....23
3.3.1 Dielectric Resonance Spectroscopy....23
3.3.2 Nonlinear Capacitance Dilatometry....27

IV. RESULTS AND DISCUSSION....30
4.1 Computational Model....30
4.2 Experimental Verification....35

V. CONCLUSION AND FUTURE WORK....38
5.1 Conclusion....38
5.2 Future Work....38

REFERENCES....39

LIST OF FIGURES

FIGURE PAGE

1.1 High electric field is applied to a cellular polypropylene sample resulting in "engineered" electric dipoles....2

1.2 Top: Direct piezoelectric effect. Bottom: Converse piezoelectric effect....3

1.3 Layered model of a ferroelectret....4

2.1 Approximation of a cellular ferroelectret film (top left) by idealized box-shaped voids (bottom left), which are then rearranged by void heights (thick stack model, right). There are a total of N classes of void heights $s_{v1} \ldots s_{vN}$....6

2.2 Scanning electron micrograph of a cellular polypropylene film from which the thickness parameters s, s_p and the void height distribution n_i were obtained. Best fit ellipses were found using ImageJ....7

2.3 Histogram of the void height distributions obtained from the mean values from six SEM micrographs....8

2.4 Experimental and calculated piezoelectric d_{33} coefficients using standard Paschen coefficients ($A = 274$ Vm^{-1}Pa^{-1}, $C = 11$ m^{-1}Pa^{-1})....9

2.5 Experimental and calculated piezoelectric d_{33} coefficients using modified Paschen coefficients ($A = 500$ Vm^{-1}Pa^{-1}, $C = 8$ m^{-1}Pa^{-1})....10

2.6 Plateau voltage profile used in the simulation....11

3.1 Gas diffusion expansion. Bottom Left: Scanning electron micrograph of an uninflated sample. Bottom Right: Micrograph of an inflated sample....14

3.2 High pressure chamber used for sample inflation....15

3.3 Sample holder which allows an electrical connection to be maintained with the sample while placed under high pressure....16

3.4 Pressure chamber....17

3.5 Capacitance versus time after a 274 kPa increase in pressure....18

3.6 Capacitance versus time after pressure is decreased from 274 kPa to atmospheric pressure....19

3.7 Top: Scanning electron micrograph of uninflated cellular pp sample. Bottom: Micrograph of inflated sample after 24 hours at a pressure of 500 kPa above atmospheric pressure and a subsequent heat treatment at 105°C for 30 seconds. ...20

3.8 Plateau voltage profile used for sample charging....21

3.9 Scanning electron micrograph of electrode damage due to surface corona discharges and dielectric breakdown of the material during the charging process....22

3.10 Capacitance versus time after a 40 kPa increase in pressure....23

3.11 Experimental Setup: Dielectric Resonance Spectroscopy....24

3.12 Dielectric spectrum with and without reference capacitor....25

3.13 Equivalent circuit used to account for stray inductances in the experimental setup. 27

3.14 The dielectric spectrum and fit for the sample charged at a pressure of 160 kPa....28

3.15 Experimental Setup: Nonlinear Capacitance Dilatometry....29

4.1 Experimental and calculated piezoelectric coefficients as a function of the pressure using modified Paschen coefficients of $A = 500\ \mathrm{Vm^{-1}Pa^{-1}}$, $C = 8\ \mathrm{m^{-1}Pa^{-1}}$, and $\gamma = 0.01$. In analogy to the experimental conditions, the space charge history was retained, i. e. the initial space charge distribution at each pressure step is set equal to the final space charge distribution at the end of the previous step. ...31

4.2 Space charge deposited for each void height as a function of the pressure, calculated using the modified Paschen coefficients listed in the caption of Fig. 4.1. Top: at $V = 6$ kV (step number 216 in Fig. 2.6); bottom: $V = 0$ V (step number 240). As in Fig. 4.1, the space charge history was retained....33

4.3 Paschen breakdown fields as a function of pressure for a range of void heights, using modified Paschen coefficients....34

4.4 Calculated piezoelectric coefficients as a function of the pressure using the modified Paschen coefficients listed in the caption of Fig. 4.1 and assuming the space charge is zero at each pressure step....35

4.5 Space charge deposited for each void height as a function of the pressure, assuming the space charge at the beginning of each pressure step is zero, calculated using modified Paschen coefficients listed in the caption of Fig. 4.1. Top: at $V = 6$ kV (step number 216 in Fig. 2.6); bottom: $V = 0$ V (step number 240). ..36

CHAPTER I

INTRODUCTION

This thesis is the summation of work given in oral presentations at the Conference on Electrical Insulation and Dielectric Phenomena, West Lafayette, IN, October 2010 and the 14^{th} International Symposium on Electrets, Montpellier, France, August 2011 and a paper, *Pressure Dependence of Space Charge Deposition in Piezoelectric Polymer Foams: Simulations and Experimental Verication*, in Applied Physics A.

Electrically charged voided polymers, so-called *ferroelectrets*, have been the subject of significant research activity in recent years [1, 2]. Due to their high piezoelectric d_{33} coefficients (up to 1400 pC/N have been reported [3], although several hundred pC/N are more typical [4, 5]), their mechanical flexibility and their capability to cover large areas, they are ideally suited for a wide range of sensor and actuator applications. Due to its easy processability, cellular polypropylene (PP) has long been the "workhorse" material, despite its limited thermal stability (stored space charge begins to decay above 50°C although reduced space-charge levels can be maintained if the material has been subjected to a pre-aging procedure [6]). In recent years, several other materials and systems based on charge storage in internal voids have been presented, such as polyethylene terephthalate and polyethylene naphthalate voided in supercritical carbon dioxide [7, 8], open-porous fluoropolymer sandwiches [9], and various templated structures [10, 11].

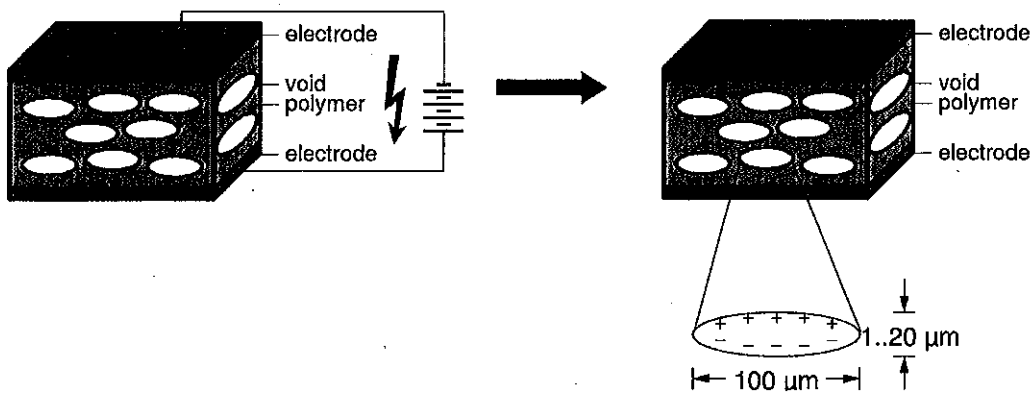

Figure 1.1. High electric field is applied to a cellular polypropylene sample resulting in "engineered" electric dipoles.

1.1 Piezoelectric Properties

The piezoelectric activity of ferroelectrets results from space charges deposited on the internal surfaces of the voids, which form "engineered" electric dipoles. Charges are created inside the voids by applying a high electric field to the foam in the direction perpendicular to the film surface. When the electric field in the gas-filled voids exceeds the critical field E_c for Paschen breakdown, dielectric barrier discharges occur in cylindrical channels 10 to 100 µm in diameter and lasting a few tens of nanoseconds [12], generating charge pairs that are separated and trapped at the internal surfaces of the voids as shown in Fig. 1.1. These electric dipoles give rise to the piezoelectric properties of the material. When the charged cellular polypropylene material is compressed, the polarization per volume of the sample is changed which results in an electric potential across the surface electrodes as shown in Fig. 1.2 top. Conversely, applying a voltage to the surface electrodes produces a mechanical response in the material as shown in Fig. 1.2 bottom. These

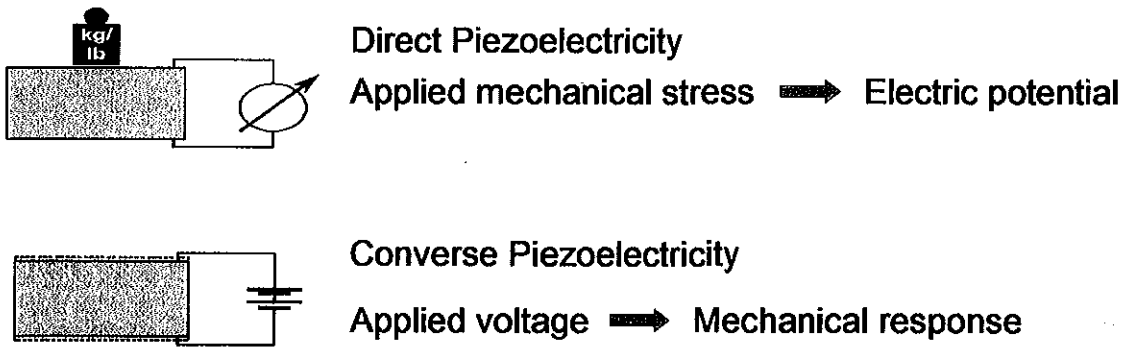

Figure 1.2. Top: Direct piezoelectric effect. Bottom: Converse piezoelectric effect.

effects are known as the direct and converse piezoelectric effect respectively and are characterized by the piezoelectric d_{33} coefficient and other electrical, electromechanical, and electric properties of the material.

1.2 Model

There have been several attempts to model the piezoelectricity of ferroelectrets. A key parameter to characterize the charging process of a ferroelectret is the space charge density σ deposited into the voids. A widely used model developed by Sessler *et al.* [13, 14] and Paajanen *et al.* [15, 16] treats the ferroelectrets as a layered system of alternating polymer layers with thicknesses s_{pi} and gas layers with thicknesses s_{vi} as shown in Fig. 1.3. It is assumed that there is no volume charge and that the total surface charge densities on opposing dielectric barriers are equal in magnitude, but opposite in sign. This model formed the basis for several later studies, which successfully modeled the experimentally observed hysteresis behavior [17] of σ as a function of the charging voltage V for both open-porous materials (with only a single void height) [18, 19] and closed-cell materials with a distribution of void heights [20]. In the present work, the latter work is extended

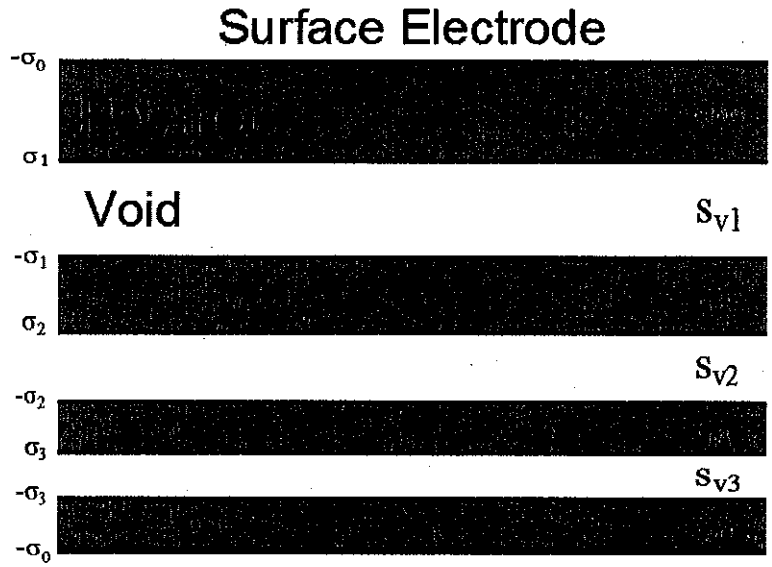

Figure 1.3. Layered model of a ferroelectret.

to find the space-charge density in the closed cells as a function of both void height and pressure, and to determine the optimal pressure for charging ferroelectrets.

CHAPTER II

MODELING THE CHARGING PROCESS

2.1 Electromechanical Model

The sample is approximated by first treating the internal ellipsoidal voids within the ferroelectret film as idealized box shaped voids as shown in Fig. 2.1. Then, to obtain an average over a large number of void sizes, a "thick stack" of alternating polymer layers (thickness s_{pi}, $i = 1 \ldots N+1$) and gas-filled voids (thickness s_{vi}, $i = 1 \ldots N$) is created, also shown in Fig. 2.1. The index i denotes the different classes of void heights with n_i voids in each class. There is space charge σ_i on the internal surfaces of voids of height s_{vi}. If a voltage V is applied to the surface electrodes of the film the resulting internal electric fields can be calculated by applying Gauss' law to each void/polymer interface and by applying Kirchoff's loop rule to the entire stack.

In order to obtain a realistic distribution of void heights, six scanning electron micrographs (taken with a JEOL JSM-840A scanning electron microscope) were taken from two cellular polypropylene samples, such as shown in Fig. 2.2. The SEM images were subsequently analyzed using ImageJ, an image processing program, to find best fit ellipses to the voids and then taking the average of the void height distributions as shown in Fig. 2.3. In order to account for the fact that voids with a smaller horizontal size are more densely packed in the film's plane, the number of voids of each void height class, n_i, was weighted with the horizontal size of the voids.

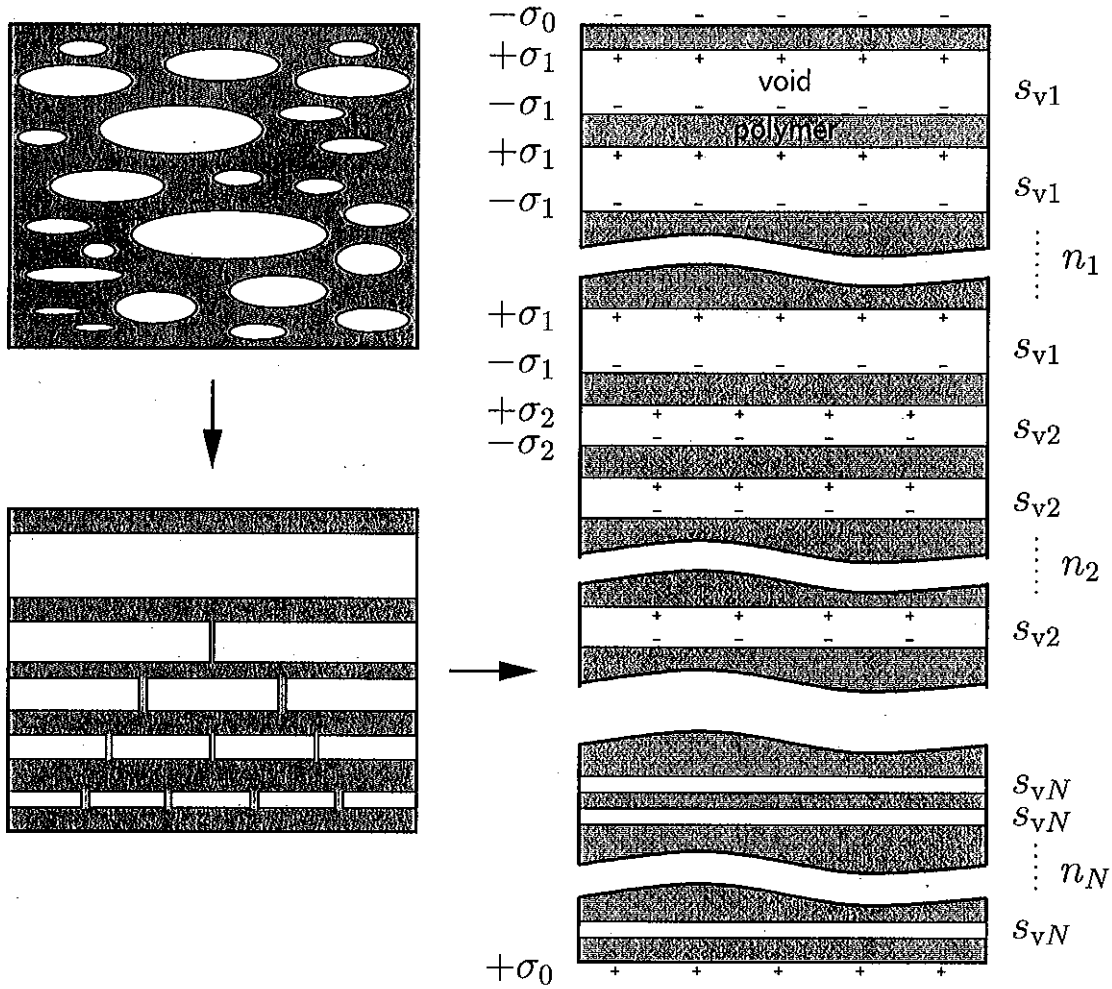

Figure 2.1. Approximation of a cellular ferroelectret film (top left) by idealized box-shaped voids (bottom left), which are then rearranged by void heights (thick stack model, right). There are a total of N classes of void heights $s_{v1} \ldots s_{vN}$.

Recently published work [20] has shown that when using the standard Paschen coefficients for air ($A = 274$ Vm^{-1}Pa^{-1}, $C = 11$ m^{-1}Pa^{-1}) the onset of piezoelectric activity is predicted to occur at much lower voltages than is experimentally seen as shown in Fig. 2.4. However, by using modified Paschen coefficients of $A = 500$ Vm^{-1}Pa^{-1} and $C = 8$ m^{-1}Pa^{-1} there is good agreement between the predicted behavior and experimental

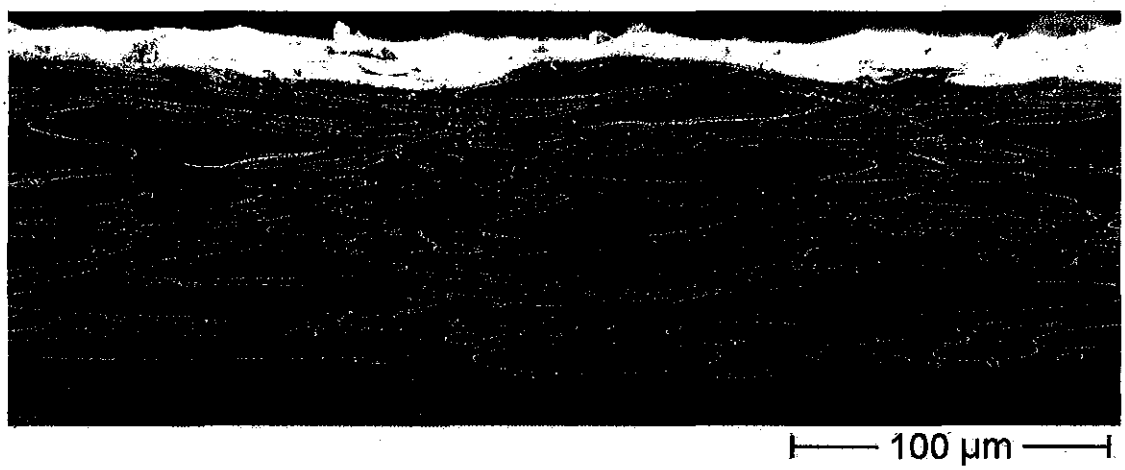

Figure 2.2. Scanning electron micrograph of a cellular polypropylene film from which the thickness parameters s, s_p and the void height distribution n_i were obtained. Best fit ellipses were found using ImageJ.

data as shown in Fig. 2.5. This suggests that the standard Paschen curves may not apply for dielectric barrier discharges in micrometer sized voids hence the modified coefficients were used for all calculations in this study.

As has been previously shown [13], the electric field E_p is the same in all of the polymer layers. The electric fields in the void height classes, n_i, however, depend upon the amount of space charge, σ_i, that has been deposited in each height class. If the internal surfaces carry a space charge density σ_i, applying Gauss' law to each polymer/void interface yields

$$\varepsilon_p E_p - E_{vi} = \sigma_i/\varepsilon_0 \tag{2.1}$$

where $\varepsilon_p = 2.2$ is the dielectric constant of the polymer. The electric fields in the voids E_{vi} and in the polymer E_p are related to an externally applied voltage V_m via Kirchhoff's loop

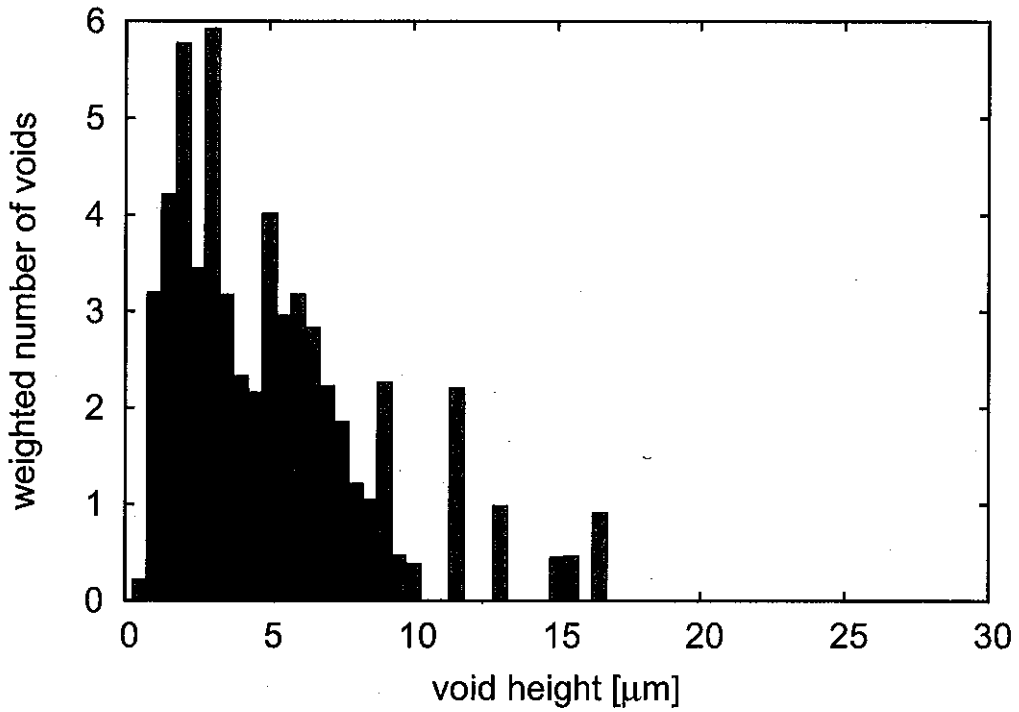

Figure 2.3. Histogram of the void height distributions obtained from the mean values from six SEM micrographs.

rule

$$\sum_{i=1}^{N} n_i s_{vi} E_{vi} + E_p \sum_{i=1}^{N+1} n_i s_{pi} = V_m \tag{2.2}$$

Due to the vertical stacking of the n_i voids of height s_{vi}, the resulting model film is much thicker than the real material. If the thickness of the actual inflated material is s and the thickness of the polymer layers is s_p (i.e. the uninflated sample thickness), then the total thickness of the void layers is given by $s_v = s - s_p$. However, the "thick stack" model yields a total void thickness of

$$s_{vm} = \sum_i n_i s_{vi}\,, \tag{2.3}$$

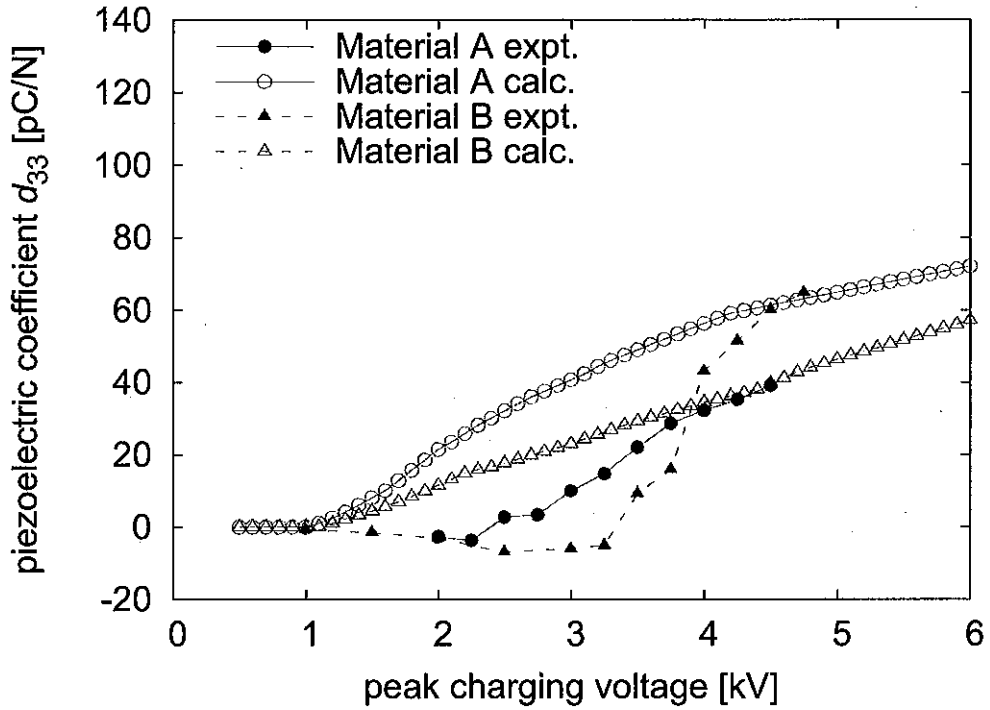

Figure 2.4. Experimental and calculated piezoelectric d_{33} coefficients using standard Paschen coefficients ($A = 274$ Vm^{-1}Pa^{-1}, $C = 11$ m^{-1}Pa^{-1})[20].

which is a factor of $\frac{s_{vm}}{s_v}$ larger than the actual film thickness. Therefore, in order to preserve the proportions and electric fields, the combined polymer layer thickness and the applied voltage are scaled by a factor of

$$\alpha = \frac{\sum_i n_i s_{vi}}{s - s_p}, \tag{2.4}$$

i. e. $V_m = \alpha V$ and $s_{pm} = \alpha s_p$. Hence, Eq. (2.2) can be written as

$$\sum_{i=1}^{N} n_i s_{vi} E_{vi} + E_p s_{pm} = V_m. \tag{2.5}$$

The piezoelectric coefficient can then be calculated as the change in the compensation charge on the surface electrodes, $\Delta\sigma_0$, due to an applied mechanical stress.

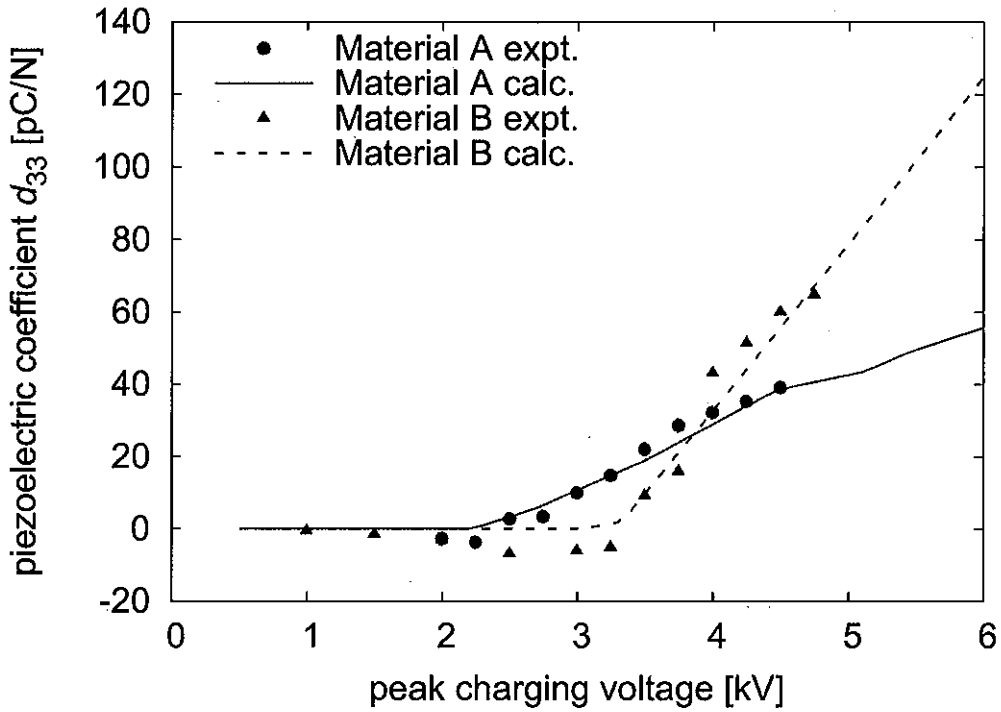

Figure 2.5. Experimental and calculated piezoelectric d_{33} coefficients using modified Paschen coefficients ($A = 500$ Vm^{-1}Pa^{-1}, $C = 8$ m^{-1}Pa^{-1})[20].

2.2 Computational Algorithm

In the present simulation, 61 void height classes were used ranging from 0 to 30 μm in 0.5 μm increments and the following calculations were performed:

1. The applied voltage V is changed in small steps of 260 V or less according to the "plateau"-like profile of Fig. 2.6 starting with an uncharged sample at $V = 0$ (i.e. $\sigma_i = 0$ for all i). After each step, the electric fields E_{vi} in each void class is calculated according to

$$E_{vi} = \frac{\varepsilon_p}{s_{pm} + \varepsilon_p s_{vm}} \left(V_m + \frac{1}{\varepsilon_0} \sum_i n_i s_{vi} \sigma_i \right) - \frac{\sigma_i}{\varepsilon_0}. \tag{2.6}$$

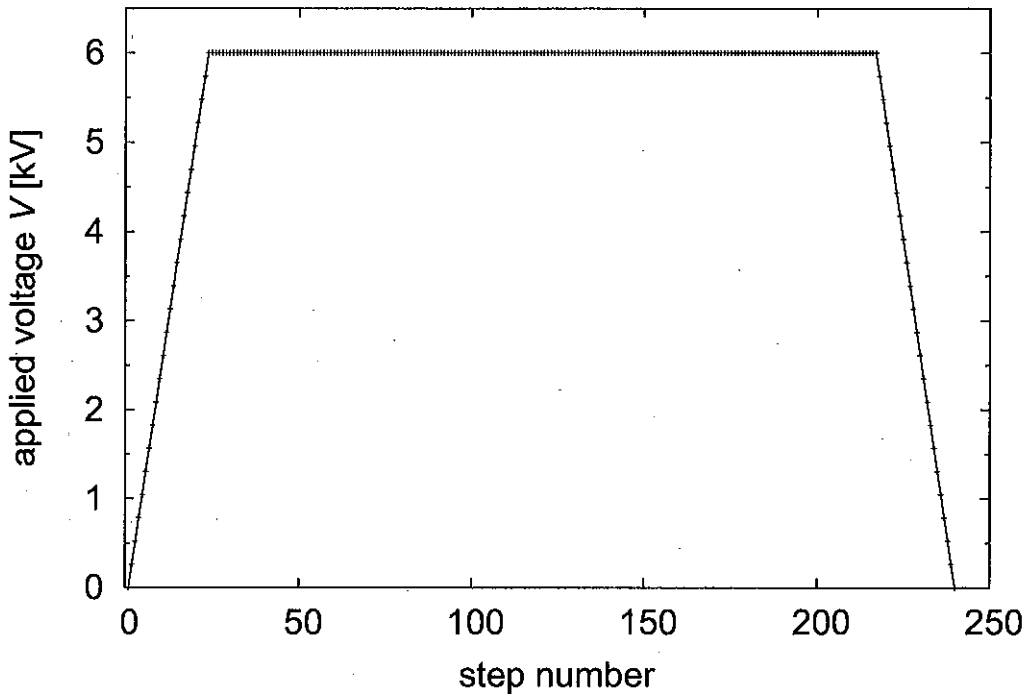

Figure 2.6. Plateau voltage profile used in the simulation.

2. The field in each void height class, E_{vi}, is compared to the critical breakdown field E_{ci} for that void height as predicted by Townsend's model of Paschen breakdown [21], i. e.

$$E_{ci} = \frac{Ap}{B + \ln(ps_i)} \tag{2.7}$$

where p is the gas pressure and

$$B = \ln\left(\frac{C}{\ln(1+1/\gamma)}\right). \tag{2.8}$$

3. If $E_{vi} > E_{ci}$ breakdown events occur, charges are separated and deposited on the polymer surfaces of voids of height s_{vi} thus changing the space charge density. Previous studies [9, 19, 20] have shown that the amount of added space charge is just sufficient to bring the electric field down to just below the Paschen breakdown threshold hence the space charge is calculated according to

$$\sigma_i' = \sigma_i + \varepsilon_0(E_{vi} - E_{ci}). \tag{2.9}$$

4. This change in deposited space charge for any one void class results in a change in the shielding of the electric field which will cause the electric field in the other void classes and the polymer layers to increase as shown by Kirchoff's loop rule (Eq. (2.2)). These changes in the fields can result in further breakdown events occurring. Therefore to ensure that equilibrium has been reach before proceeding to the next voltage step, steps 2-3 are repeated until no further breakdown events occur.

5. After equilibrium in all void classes has been reached, the applied voltage V is changed again, and steps 1-4 are repeated until the last step of the voltage profile in Fig. 2.6 has been reached.

6. When V has reached 0 V at the end of the charging cycle, the piezoelectric coefficient can be obtained via

$$d_{33} = \frac{s_{pm} + s_{vm}}{Y} \cdot \frac{-\varepsilon_0 \varepsilon_p^2 V + \dfrac{\varepsilon_p s_{pm}}{s_{vm}} \sum_i n_i s_{vi} \sigma_i}{(s_{pm} + \varepsilon_p s_{vm})^2}. \tag{2.10}$$

7. Steps 1-6 are then repeated for a range of pressures from 51 kPa to 396 kPa. For each pressure, the initial charge distribution is set to $\sigma_i = 0$.

   In a variation of the above process, the initial space charge distribution at each pressure step is set equal to the final space charge distribution at the end of the previous step. This corresponds to repeatedly charging a single sample over a range of pressures, thus requiring the space charge history from prior charging to be tracked.

CHAPTER III

EXPERIMENT

3.1 Sample Preparation

3.1.1 Sample Inflation

The material used in this study was a commercially available cellular polypropylene film from Nan Ya Plastics Corp., Taipei, Taiwan designated PQ-50. In order to create the lens-like voids necessary to produce engineered dipoles and to increase the thickness elasticity of the sample, the material was inflated using a two-step gas diffusion expansion [22, 23]. A uninflated sample, as shown in the scanning electron micrograph in Fig. 3.1 bottom left, with a thickness of 50 μm was first put into dry nitrogen gas at high pressure in a pressure chamber, shown in Fig. 3.2, resulting in the external pressure being much larger than the internal pressure (which will begin at atmospheric pressure). Due to this pressure

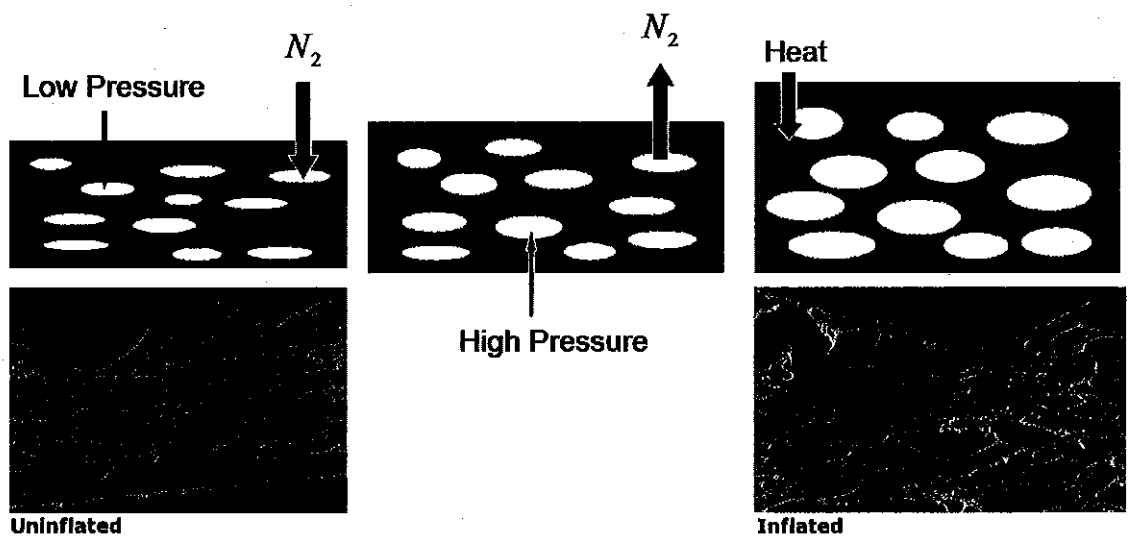

Figure 3.1. Gas diffusion expansion. Bottom Left: Scanning electron micrograph of an uninflated sample. Bottom Right: Micrograph of an inflated sample.

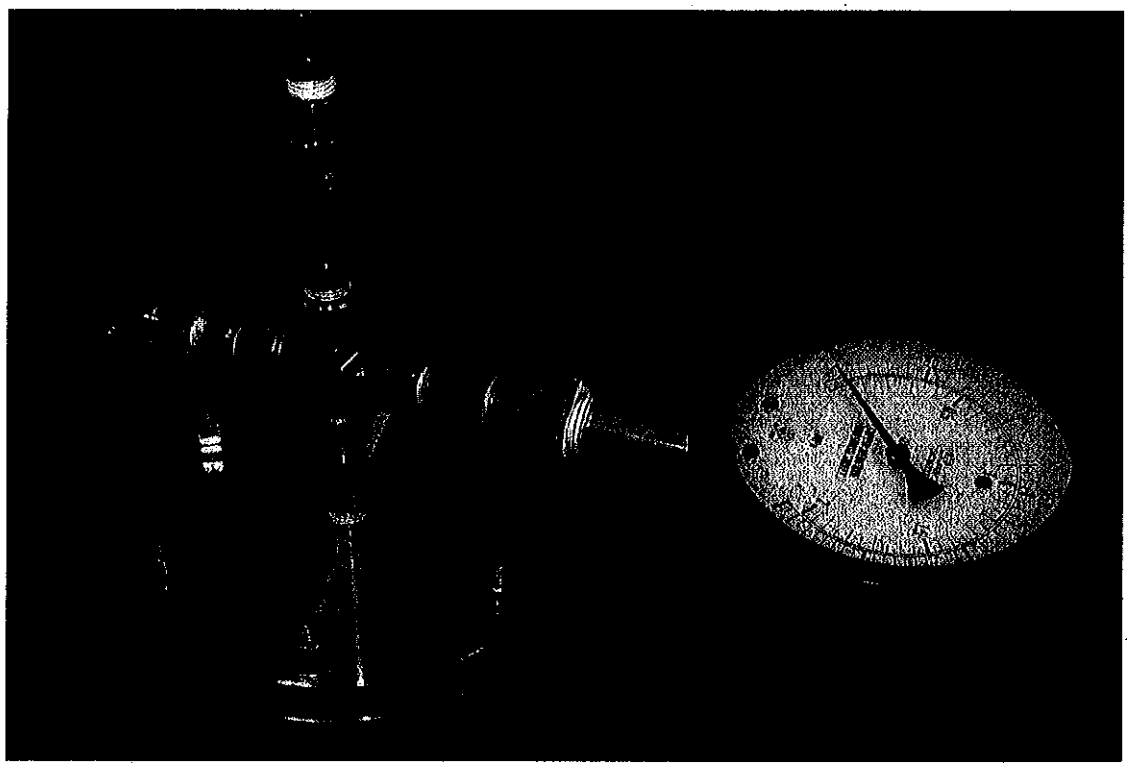

Figure 3.2. High pressure chamber used for sample inflation.

difference the nitrogen gas diffuses into the sample causing it to expand. This expansion continues until the pressures within and without the sample reach equilibrium as shown in Fig. 3.1 center. After equilibrium is reached, the sample is returned to atmospheric pressure resulting in an internal pressure much greater than the external pressure causing further expansion of the sample. Again, due to the pressure difference, the nitrogen gas will now begin to diffuse out of the material causing the thickness to be reduced. In order to prevent this reduction of sample thickness, the sample is given a subsequent heat treatment, softening the material and allowing it to expand further until the internal and external pressures are equalized resulting in an inflated sample as shown in the SEM micrograph in Fig. 3.1 bottom right.

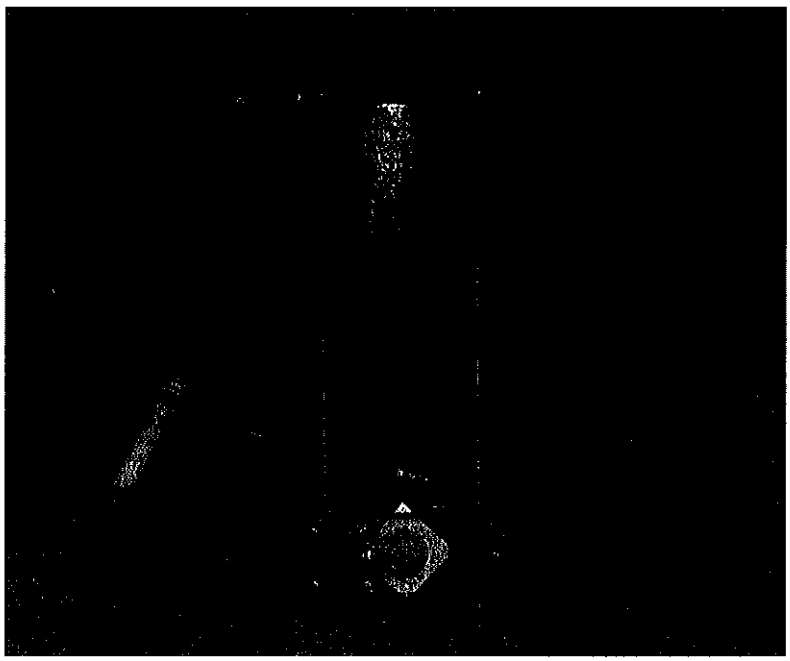

Figure 3.3. Sample holder which allows an electrical connection to be maintained with the sample while placed under high pressure.

3.1.2 Dilatometry

In order to determine the amount of time required for the pressures to reach equilibrium after the external pressure is changed, dilatometry studies were performed. Electrodes were placed on the sample surfaces using physical vapor deposition resulting in two electrodes separated by a dielectric medium which allows the sample to be modeled as a parallel plate capacitor with capacitance $C = \frac{\varepsilon_r A}{d}$ where ε_r, A and d are the relative permittivity of the material, the electrode area, and the distance between the electrodes respectively. As the gas diffuses into or out of the material, the change in sample thickness will result in a corresponding change in the sample capacitance. Therefore by measuring the capacitance during the inflation process, the sample thickness and state of pressure equilibrium can be determined.

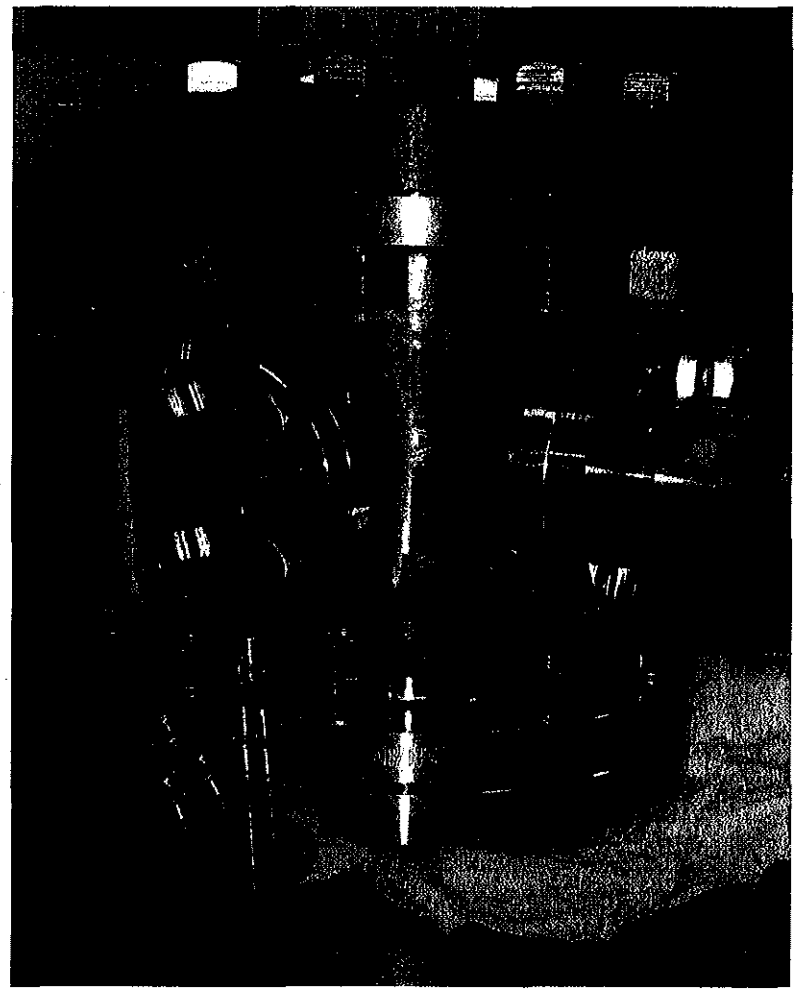

Figure 3.4. Pressure chamber.

A sample of the cellular PP material was mounted in a sample holder shown in Fig. 3.3 and sealed in a pressure chamber as shown in Fig. 3.4 allowing for it to be pressurized. The sample was then placed under a pressure of 274 kPa for 24 hours while the capacitance was measured using a Agilent 4294A impedance analyzer. As can be seen in Fig. 3.5, placing the sample under high pressure causes it to be compressed thus increasing the capacitance. As the gas diffuses into the material, the sample expands, resulting in a

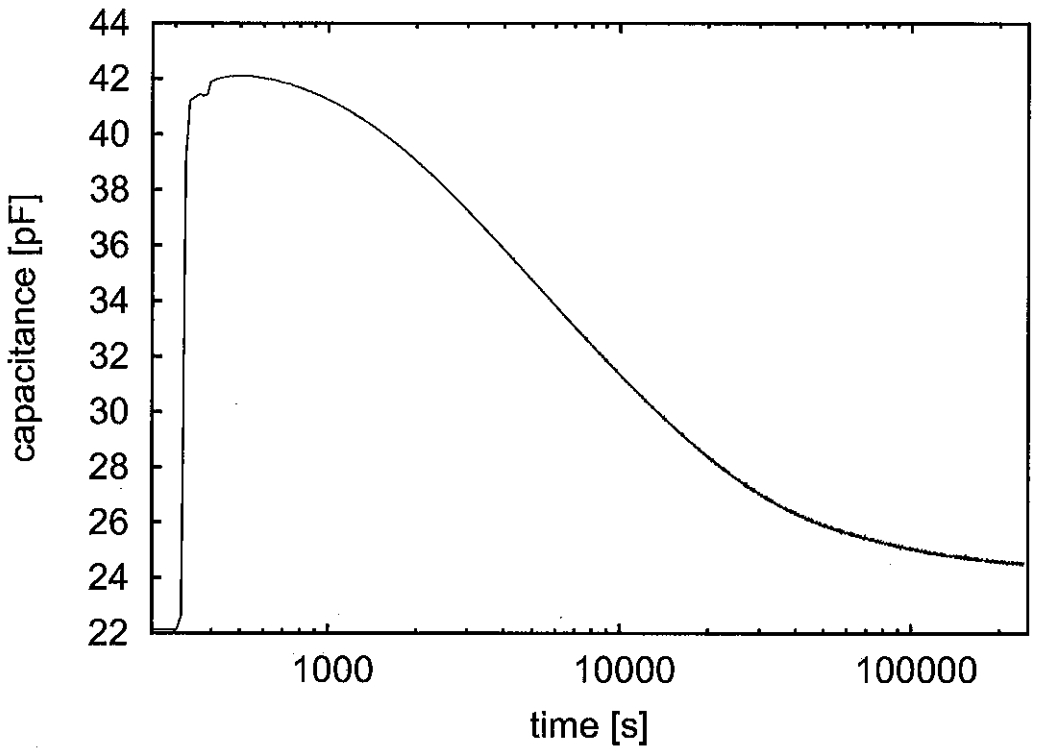

Figure 3.5. Capacitance versus time after a 274 kPa increase in pressure.

corresponding reduction of the capacitance. From this it was determined that 24 hours is sufficient time for the pressures within and without the sample to approach equilibrium.

The sample was then returned to atmospheric pressure resulting in an expansion of the material and corresponding reduction of the capacitance as shown in Fig. 3.6. As the high pressure internal gases diffuse out of the sample, the sample thickness decreases resulting in an increase in the capacitance. From this it was determined that during the approximately 2 minutes required for the sample to be removed from the pressure chamber and subsequently heat treated no significant decrease in sample thickness occurs.

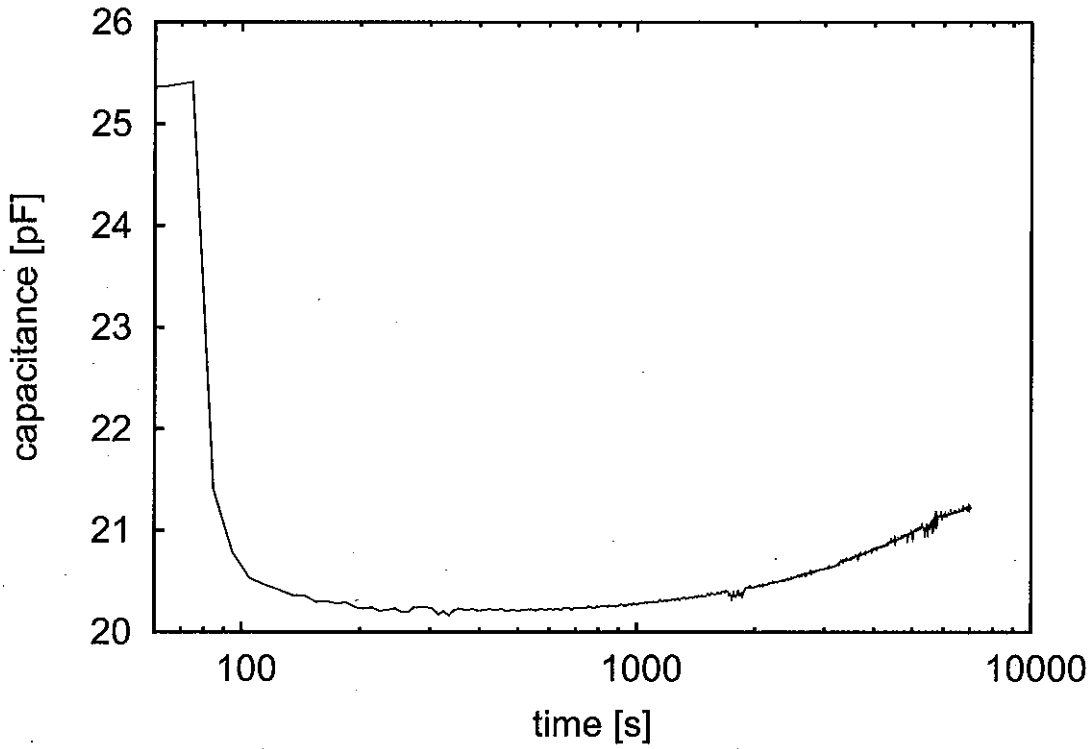

Figure 3.6. Capacitance versus time after pressure is decreased from 274 kPa to atmospheric pressure.

From these studies, inflation parameters of 500 kPa for 24 hours and a subsequent heat treatment at 105°C were chosen resulting in inflated sample thicknesses ranging from 80 μm to 90 μm as shown in Fig. 3.7.

3.2 Sample Charging

In order to apply a charging voltage across the sample and subsequently measure the dielectric spectrum, 25 nm thick circular gold electrodes with 16 mm diameter were coated on the sample surfaces using physical vapor deposition.

To minimize the effects of sample-to-sample variations in the distribution of void heights, a single sample was used and repeatedly charged as the pressure was increased.

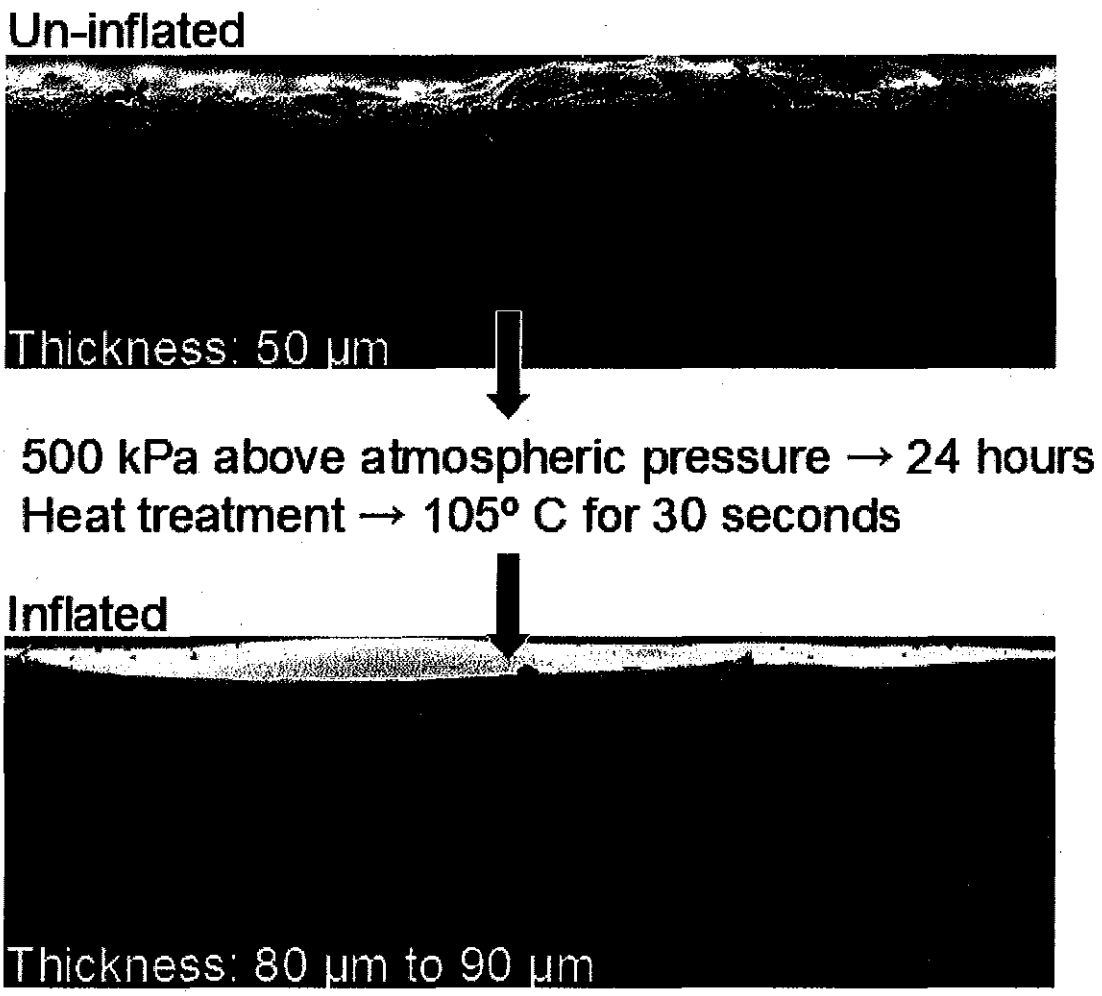

Figure 3.7. Top: Scanning electron micrograph of uninflated cellular pp sample. Bottom: Micrograph of inflated sample after 24 hours at a pressure of 500 kPa above atmospheric pressure and a subsequent heat treatment at 105°C for 30 seconds.

Additionally, this procedure this procedure allows the measurements to be completed in a single day, thus avoiding viscoelasticity-induced changes in the d_{33} coefficient [24]. The sample was charged in a dry nitrogen atmosphere at pressures from 61 kPa to 381 kPa. The pressure was raised in 20 kPa increments until atmospheric pressure was reached, and then increased in 40 kPa increments. A plateau charging voltage profile (analogous to

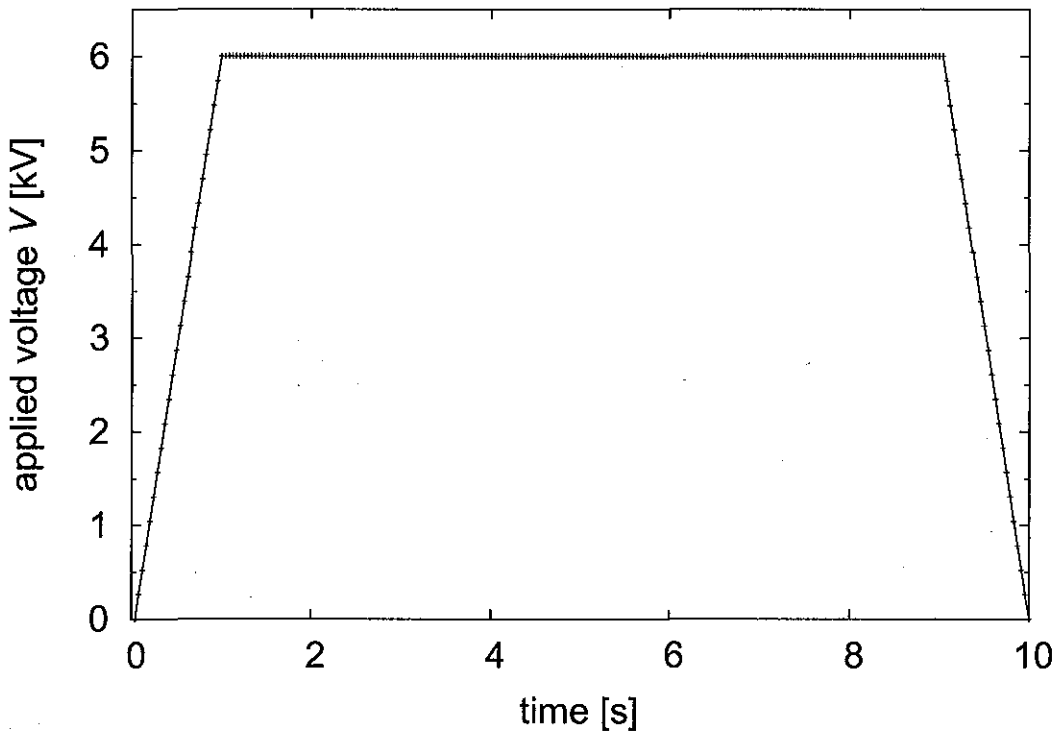

Figure 3.8. Plateau voltage profile used for sample charging.

the charging profile used in the simulations) shown in Fig. 3.8 was applied to the sample using an Agilent 33220A arbitrary waveform generator and a Matsusada AMT-20B10 high voltage amplifier. As individual barrier discharge events occur on a time scale of 100 ns or less [25], this profile implies charging under quasi-constant voltage, in agreement with our numerical model.

Attempts were made to charge a variety of cellular polypropylene films as shown in Tab. 3.1. However, corona discharges on the surface electrodes and eventual breakdown of the dielectric material occurred, resulting in sample damage as shown in Fig. 3.9 which prevented their use in this study. The ability to charge the PQ-50 PP films without the occurrence of surface discharges led to its selection for use in this study.

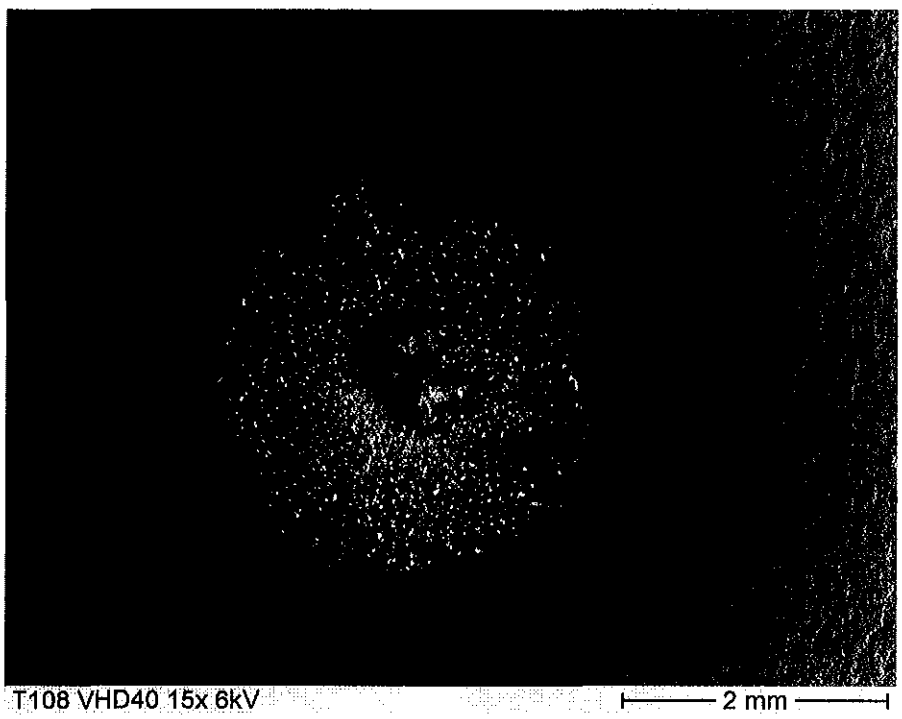

Figure 3.9. Scanning electron micrograph of electrode damage due to surface corona discharges and dielectric breakdown of the material during the charging process.

Table 3.1. The material PQ-50 was used in this study. The other materials experienced corona discharges and dielectric breakdown during charging.

Manufacturer	Film Name
Nan Ya Plastics Corp., Taipei, Taiwan	PQ-50
Emfit Ltd, Vaajakoski, Findland	HS-03-20BR
Treofan, Neunkirchen, Germany	VHD 40, EUH 70, SHD 50, SHD 60

The sample was initially placed under a low vacuum at a pressure of 61 kPa. After 1 hour the sample was charged and the dielectric spectrum measured using a Agilent 4294A impedance analyzer. Again, in order to determine if the interior and exterior pressures had sufficiently approached equilibrium, dilatometry data was recorded after each pressure change. As can be seen in Fig. 3.10 after one hour the sample had approached hydrostatic

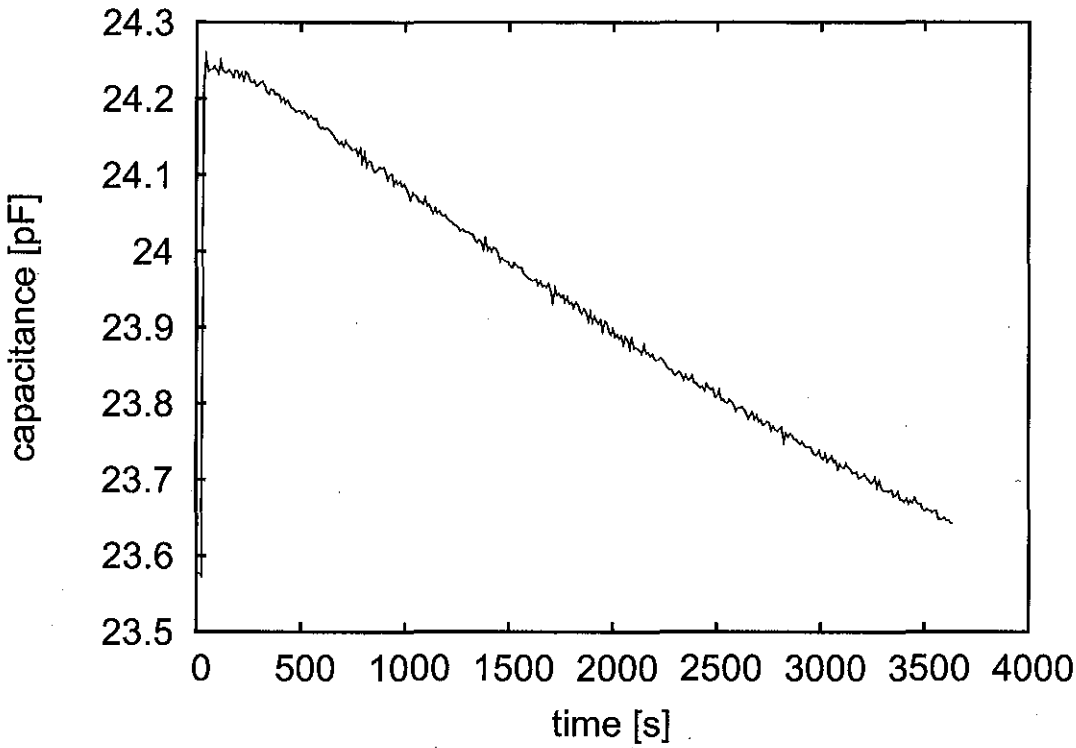

Figure 3.10. Capacitance versus time after a 40 kPa increase in pressure.

equilibrium by ninety percent. The pressure was then increased and the process repeated up to a pressure of 381 kPa.

3.3 Measurement of Piezoelectric Coefficient

3.3.1 Dielectric Resonance Spectroscopy

Dielectric spectroscopy is a well established experimental measurement technique. When a varying electric field is applied to a sample over a range of frequencies, the field interacts with dipoles within the material producing a dielectric response. This dielectric response is measured as the complex capacitance as a function of frequency using an

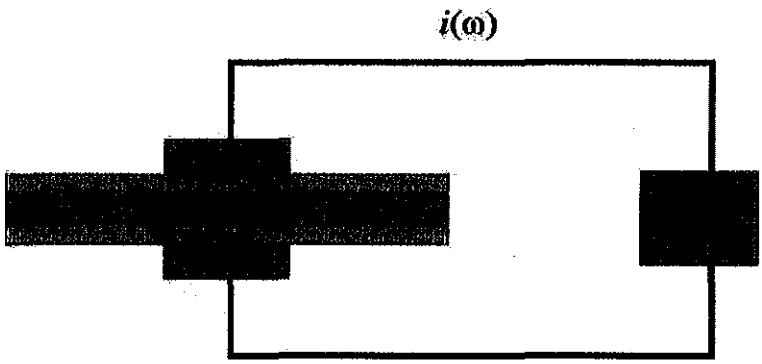

Figure 3.11. Experimental Setup: Dielectric Resonance Spectroscopy.

impedance analyzer. Electrical, electromechanical, and mechanical properties of the material such as the electronic polarization, ionic polarization, dipole relaxation, and ionic relaxation can then be determined from the spectrum.

In piezoelectric materials, the varying applied electric field interacts with dipoles within the material, causing changes in the sample thickness and corresponding changes in the dipole density, producing piezoelectric resonances in the dielectric spectrum [26, 27]. The dielectric spectrum of a material can be measured by using an impedance analyzer to apply the vary electric field over a range of frequencies while measuring the complex capacitance, as shown in Fig. 3.11. This technique has several advantages. It uses standard dielectric spectroscopy equipment commonly found in research laboratories. It also allows for in situ measurements to be made, each taking on the order of minutes, thereby eliminating the need to return the sample to atmospheric pressure. As stated earlier, viscoelasticity-induced changes in the d_{33} coefficient make this measurement time critical. As measurements using this technique take only approximately 2 minutes, it is more suitable for our purpose than other measurement techniques such as nonlinear capacitance

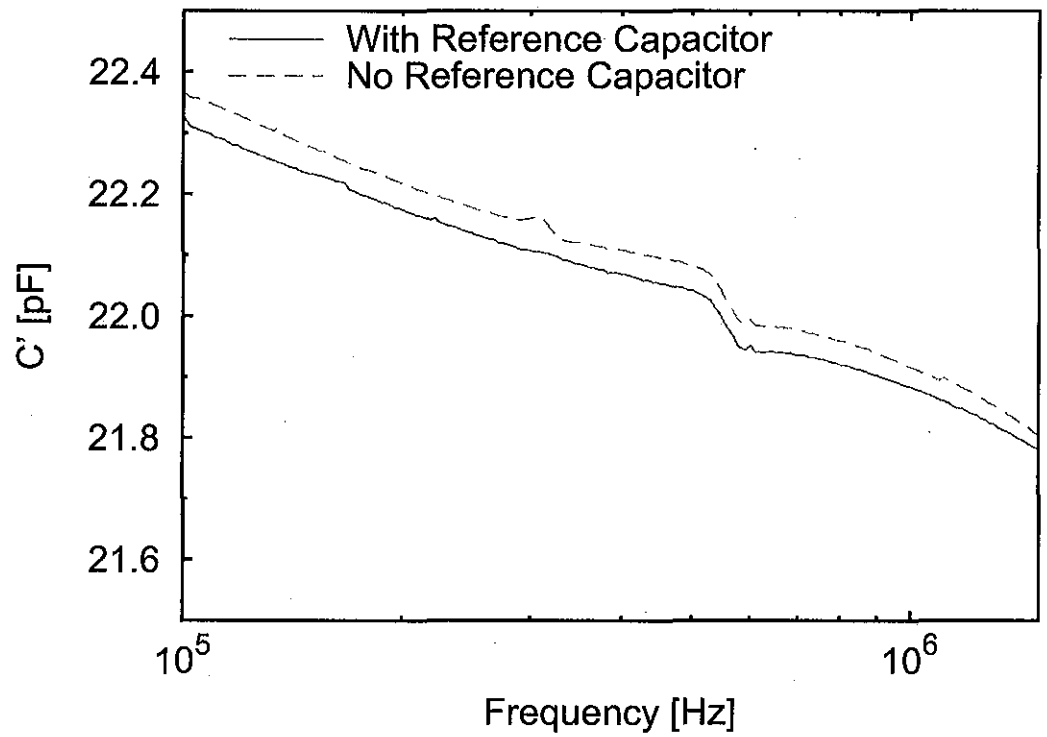

Figure 3.12. Dielectric spectrum with and without reference capacitor.

dilatometry, which takes on the order of tens of minutes. Additionally, several electrical, electromechanical, and mechanical properties of the material, such as the piezoelectric d_{33} coefficient, Young's elastic modulus, Y and the electromechanical coupling factor k_t, can be determined from a single spectrum.

In order to eliminate any instrumentation artifacts in the spectra, the dielectric spectrum of a reference capacitor with a capacitance similar to that of the sample under study was measured. Next, the spectrum of the sample was divided by the reference spectrum and then multiplied by the reference capacitance resulting in the removal of systematic artifacts as shown in Fig. 3.12.

Subsequently, a theoretical expression for the complex capacitance (see equation (84) of reference [26])

$$\tilde{C}(f) = \frac{\varepsilon A}{s} \frac{1}{1 - k_t^2 \frac{\tan(\pi f / 2 f_p)}{(\pi f / 2 f_p)}} \tag{3.1}$$

can be fit to the piezoelectric resonance in the dielectric spectrum. The piezoelectric d_{33} coefficient can then be found using Eqs. (3.2) and (3.3):

$$f_p = \frac{1}{2s} \sqrt{\frac{c_{33}}{\rho}} \tag{3.2}$$

$$d_{33}^2 = \frac{k_t^2 \varepsilon}{c_{33}}, \tag{3.3}$$

where A is the area covered by electrodes, f_p is the resonance frequency, and c_{33} is the elastic modulus.

Alternatively, in order to account for any frequency dependence of the samples capacitance, phenomenological parameters a and b can be included in the fit equation

$$C_0(\omega) = C_{00} \left\{ 1 + a \log_{10} \left(\frac{\omega}{2\pi \Re f} \right) + b \left[\log_{10} \left(\frac{\omega}{2\pi \Re f} \right) \right]^2 \right\}. \tag{3.4}$$

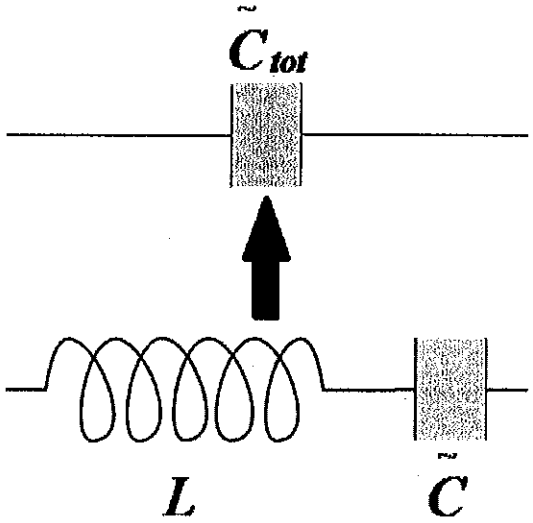

Figure 3.13. Equivalent circuit used to account for stray inductances in the experimental setup.

Additionally, stray inductances in the experimental set up can be accounted for by considering the equivalent circuit shown in Fig. 3.13 and calculating the equivalent capacitance according to

$$\tilde{C}_{tot}(\omega) = \frac{1}{-\omega^2 L + \tilde{C}(\omega)^{-1}}. \tag{3.5}$$

As an example, the dielectric spectrum and fit for the sample after being charged at a pressure of 160 kPa is shown in Fig. 3.14.

3.3.2 Nonlinear Capacitance Dilatometry

Nonlinear capacitance dilatometry is an experimental technique which allows in situ measurements of electromechanical properties of cellular polypropylene films to be made each taking on the order of tens of minutes. As explained above, this technique

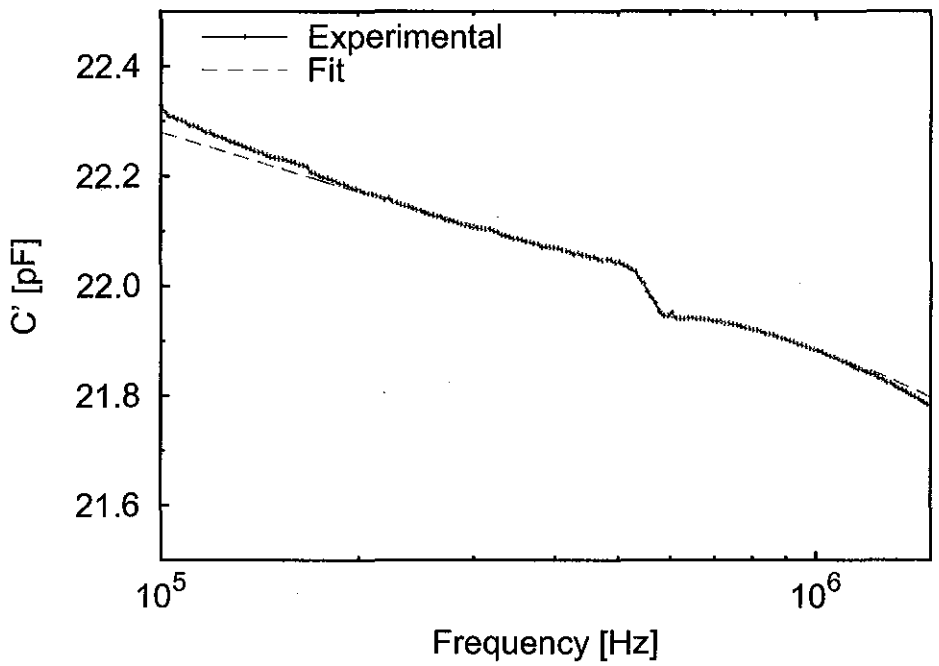

Figure 3.14. The dielectric spectrum and fit for the sample charged at a pressure of 160 kPa.

was not used in this study. When an alternating current is applied to a charged PP film, piezoelectric and electrostrictive properties of the material produce changes in the sample thickness resulting in nonlinearities in the response current from which the piezoelectric d_{33} coefficient, and Young's elastic modulus can be determined [28].

A lock-in amplifier is used to apply an A.C. signal, $V = V_0 \sin \omega t$, to a high voltage amplifier which is then applied to the polypropylene sample. The response current of the sample is then amplified using a pre-amplifier and subsequently measured by the lock-in amplifier as shown in Fig. 3.15. The zero voltage capacitance, C_0, the piezoelectric

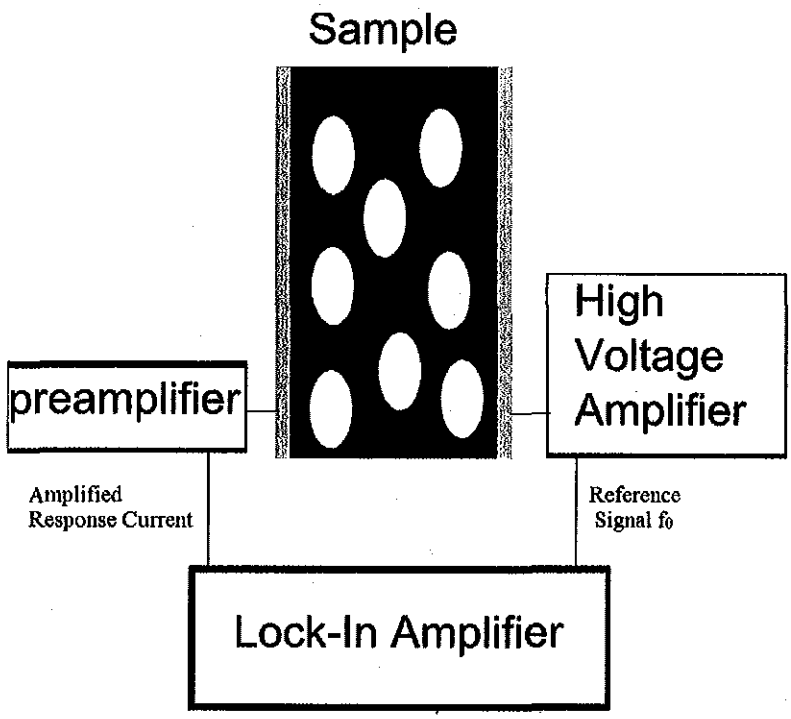

Figure 3.15. Experimental Setup: Nonlinear Capacitance Dilatometry.

coefficient, d_{33}, and Young's elastic modulus, Y can be determined from the first, second, and third harmonic of the response current respectively using

$$I = C_0 \omega V_0 \cos \omega t - \frac{C_0^2 d_{33}^0}{\varepsilon_0 A} V_0^2 \omega \sin 2\omega t + \frac{s_0 C_0^4}{2Y\varepsilon_0^2 A^3} \frac{3}{4} \cos 3\omega t \tag{3.6}$$

where A is the area of the surface electrodes and s_0 is the total thickness of the sample(see reference [28] equation (3)).

CHAPTER IV

RESULTS AND DISCUSSION

4.1 Computational Model

As explained in Chapter II the thickness parameters s, s_p and the void height distribution n_i (Fig. 2.3) were experimentally obtained from six scanning electron micrographs and modified Paschen coefficients of $A = 500$ $Vm^{-1}Pa^{-1}$, $C = 8$ $m^{-1}Pa^{-1}$, and $\gamma = 0.01$ were used for all calculations.

Charging simulations were performed using the 6 kV plateau waveform shown in Fig. 2.6 at 70 pressures ranging from 51 kPa to 396 kPa in 5 kPa increments. As stated in Chapter III a single sample was used and repeatedly charged over the range of pressures requiring the history from prior charging to be tracked as described in Chapter II. Using the optimized Paschen coefficients shown in the previous paragraph, and values of $Y = 4.0$ MPa and $\varepsilon_p = 2.2$ for Young's modulus and the permittivity of the polymer, respectively, the piezoelectric coefficient as a function of pressure was calculated as shown in Fig. 4.1. Pressures above 251 kPa were found to optimize the piezoelectric coefficient for these Paschen coefficients and charging parameters.

To investigate this behavior, the amount of space charge deposited for each void height as a function of pressure was computed at the final maximal voltage (6 kV, step number 216 in Fig. 2.6) and at the end of the charging cycle (0 kV, step number 240 in Fig. 2.6) as shown in Fig. 4.2. Smaller voids become charged as the pressure is increased,

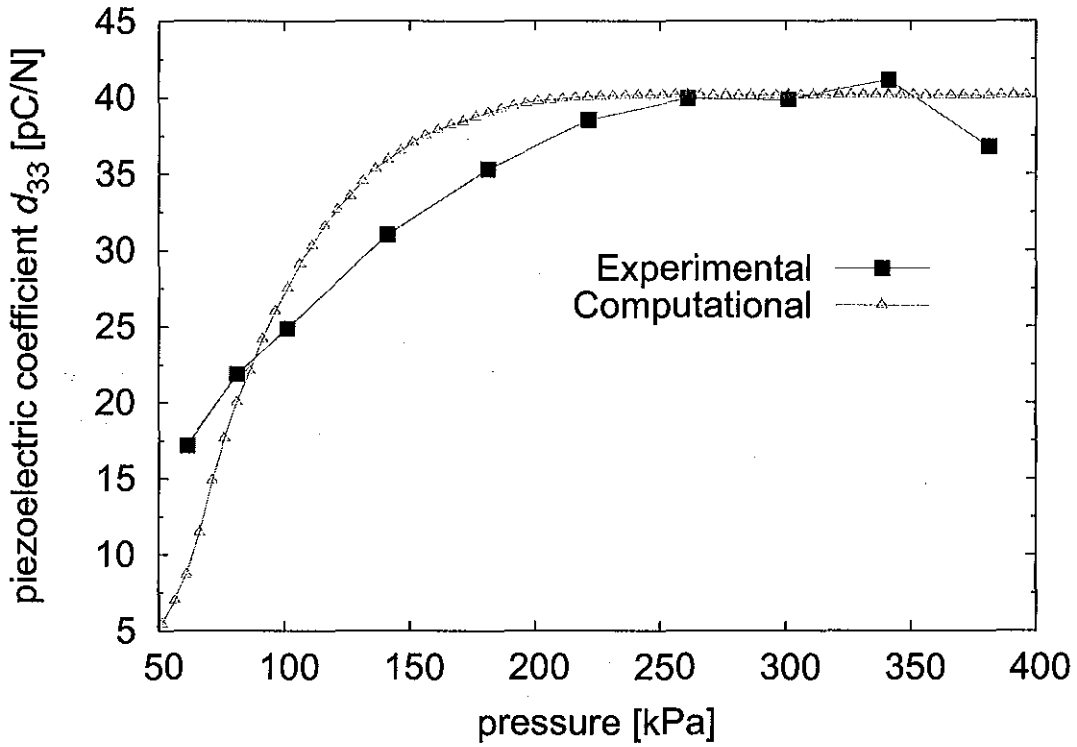

Figure 4.1. Experimental and calculated piezoelectric coefficients as a function of the pressure using modified Paschen coefficients of $A = 500$ $\mathrm{Vm^{-1}Pa^{-1}}$, $C = 8$ $\mathrm{m^{-1}Pa^{-1}}$, and $\gamma = 0.01$. In analogy to the experimental conditions, the space charge history was retained, i. e. the initial space charge distribution at each pressure step is set equal to the final space charge distribution at the end of the previous step.

resulting in an increase in the effective space charge surface density. This is easily understood by considering the Paschen breakdown field as a function of pressure as shown in Fig. 4.3 and the distribution of void heights as shown in Fig. 2.3. For void height classes smaller than approximately 14 μm, the breakdown fields as a function of pressure have minima above atmospheric pressure. For voids in this height range an increase in pressure will result in a corresponding decrease in the breakdown field, resulting in breakdown events and space charge being deposited. Figure 4.2 shows that voids in the height range of approximately 6 μm to 14 μm become charged only at higher pressures, and the void

height histogram (Fig. 2.3) shows that there are a significant number of voids in this height range in this material. Therefore, the final computed d_{33} increases as a function of pressure. However, when the pressure is increased past the minimum of the Paschen curve, the critical breakdown field begins to increase and eventually reaches values higher than the applied field. At this point, no further space charge is deposited.

A different behavior, however, is seen for voids with a height greater than approximately 14 μm which exist only in small numbers in this material. Referring again to Fig. 4.3, their breakdown field is lower than the applied field over the entire range of pressures. Hence, space charge does get deposited as the pressure increases, but in smaller amounts since the deposited space charge is proportional to the difference $E_{vi} - E_{ci}$, as shown in Eq. (2.9). Furthermore, the larger voids experience back discharges when the voltage is ramped down to 0 kV, which can be seen by comparing the top and bottom graphs of Fig. 4.2. However, increasing the pressure reduces the amount of back discharge [29], as is clearly shown in Fig. 4.2 (bottom). This results in an increase in the remaining deposited space charge at the end of the charging cycle. Therefore, the final computed d_{33} can be optimized by increasing the pressure. However, when the pressure is increased past a critical pressure (251 kPa for this material), no further space charge is deposited, and the piezoelectric activity reaches a plateau.

In most practical applications, the sample does not have a space charge history. This can be modeled by assuming that the space charge at the beginning of each pressure step is zero (i. e., a new, uncharged sample is used at each pressure). In this case, a different behavior is predicted by the model [30], as shown in Fig. 4.4. The predicted d_{33} coefficient

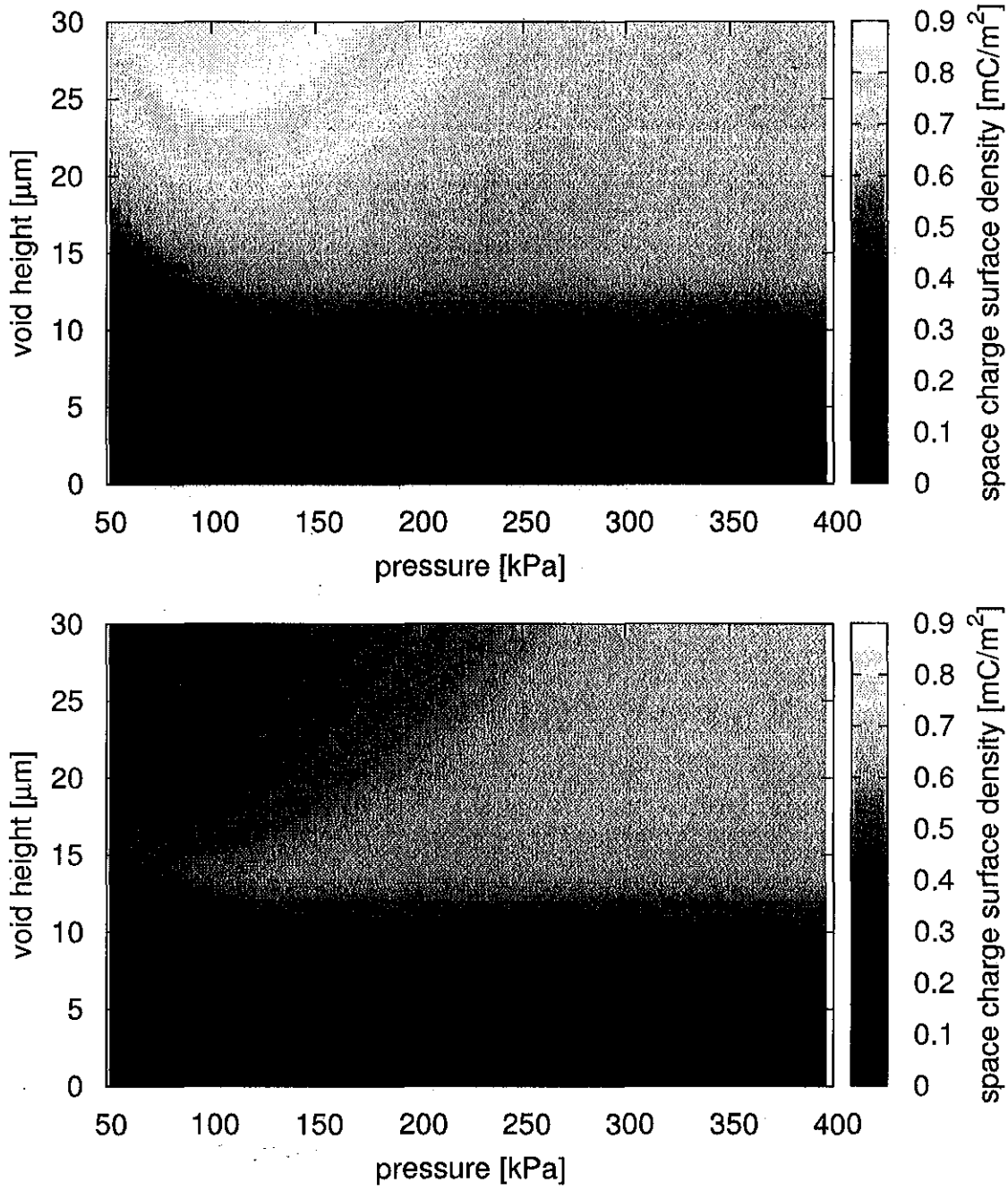

Figure 4.2. Space charge deposited for each void height as a function of the pressure, calculated using the modified Paschen coefficients listed in the caption of Fig. 4.1. Top: at $V = 6$ kV (step number 216 in Fig. 2.6); bottom: $V = 0$ V (step number 240). As in Fig. 4.1, the space charge history was retained.

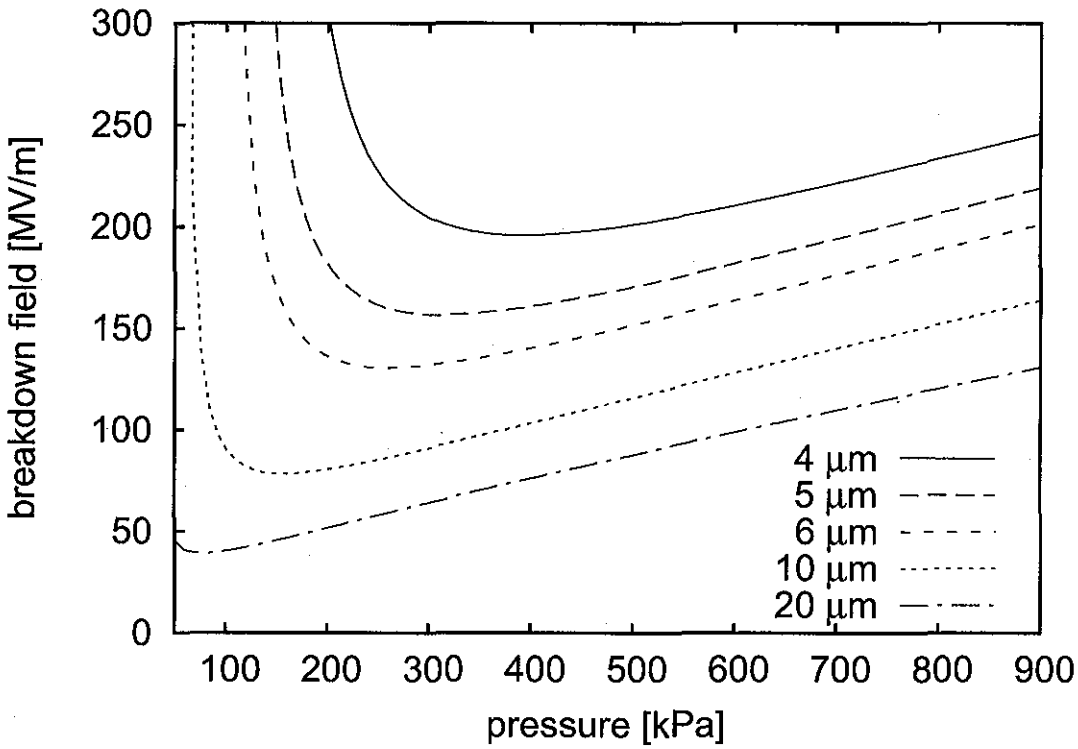

Figure 4.3. Paschen breakdown fields as a function of pressure for a range of void heights, using modified Paschen coefficients.

now reaches a maximum at 186 kPa, and is slightly lower in magnitude, 38.1 pC/N versus 40.2 pC/N. As shown in Fig. 4.5, this altered behavior can be explained by two differences from the single sample model:

1. All voids receive less charge at high pressures due to their higher breakdown fields.

2. There is no "left over" space charge from previous charging cycles.

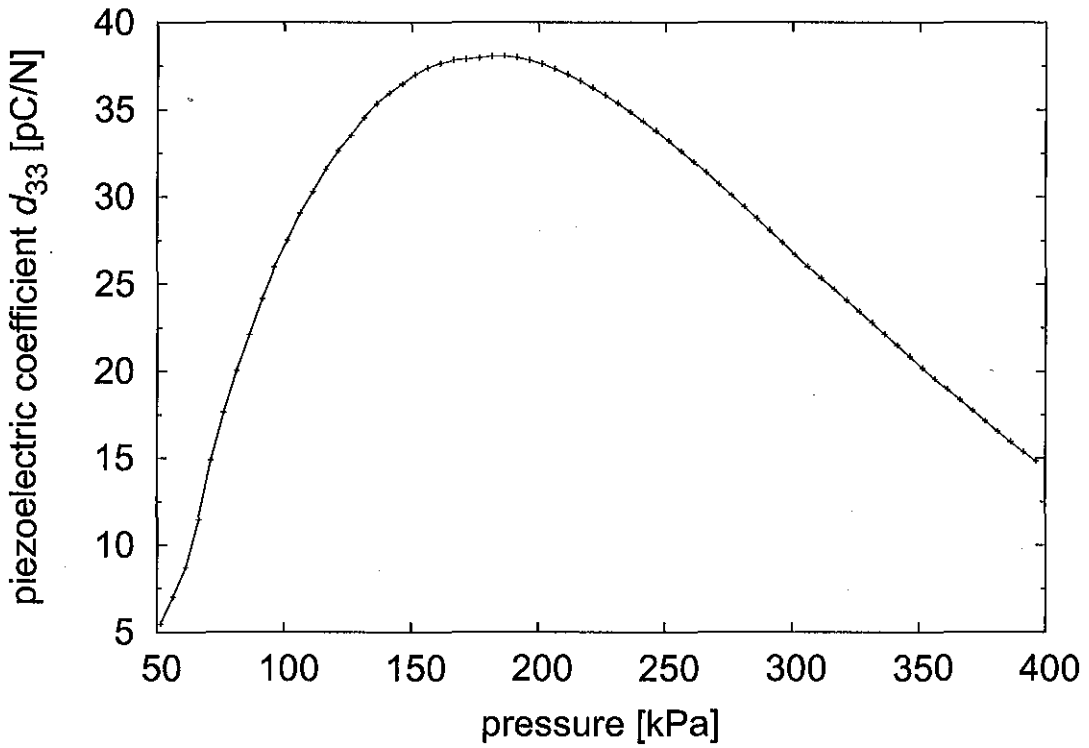

Figure 4.4. Calculated piezoelectric coefficients as a function of the pressure using the modified Paschen coefficients listed in the caption of Fig. 4.1 and assuming the space charge is zero at each pressure step.

4.2 Experimental Verification

As shown in Fig. 4.1, there is good agreement between the model prediction and the experimental measurements when the space charge history is accounted for at each pressure step in the model. The d_{33} coefficient at each pressure critically depends on the value of the breakdown field as a function of both void height and pressure which is poorly understood at present which could explain the differences seen between the experimental and computational data. Both the experimental measurements and computational predications show an increase of the d_{33} coefficient of over 40% compared to atmospheric pressure.

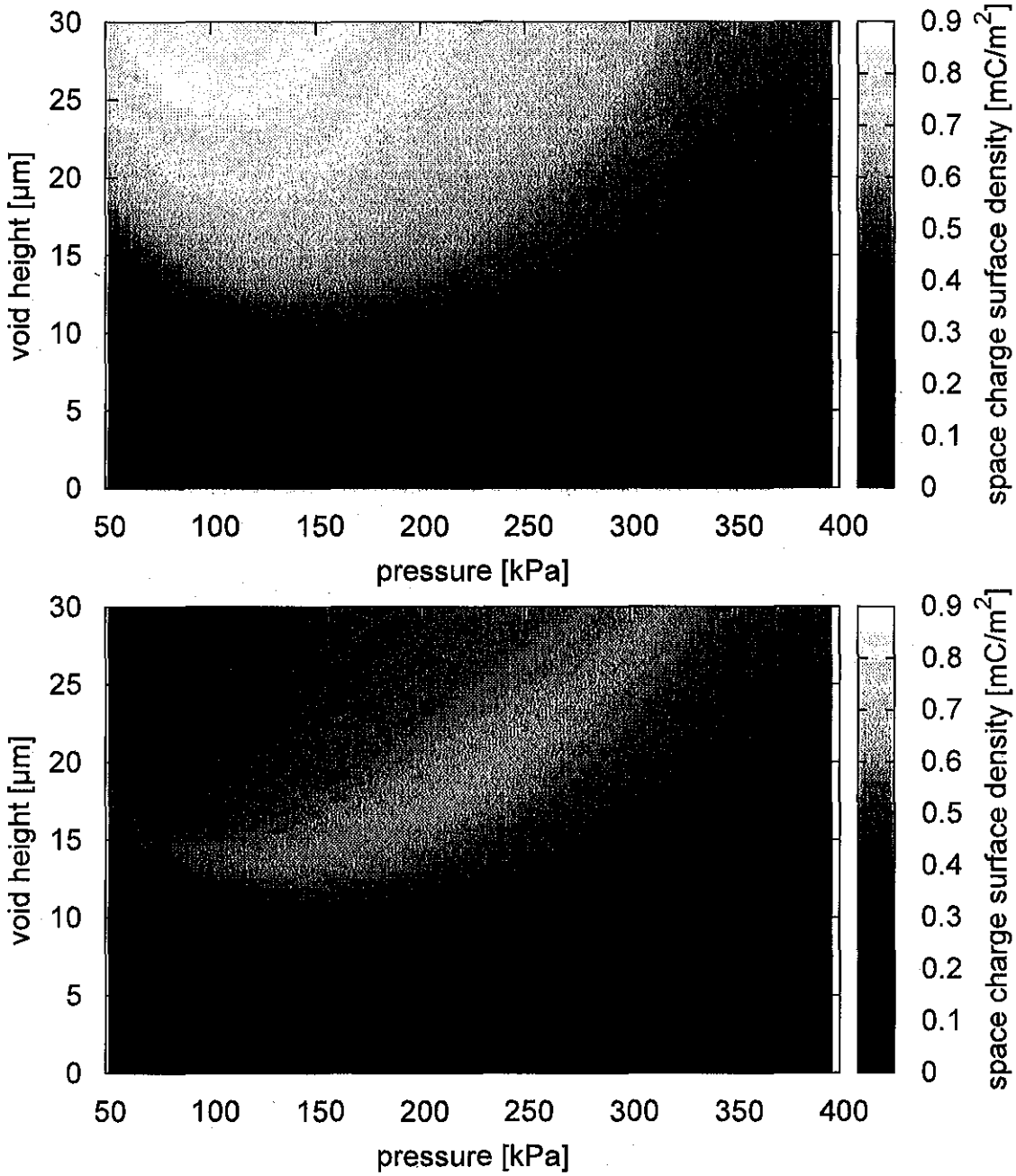

Figure 4.5. Space charge deposited for each void height as a function of the pressure, assuming the space charge at the beginning of each pressure step is zero, calculated using modified Paschen coefficients listed in the caption of Fig. 4.1. Top: at $V = 6$ kV (step number 216 in Fig. 2.6); bottom: $V = 0$ V (step number 240).

As a final check, the Maxwell stress (resulting from the attraction of the oppositely charged electrodes) was calculated. Using our electromechanical model, it can be shown that the Maxwell stress due to an applied voltage V causes a thickness change of

$$\Delta s_{\text{Maxwell}} = \left(\frac{s_p + s_v}{Y}\right) \frac{-\frac{1}{2}\varepsilon_0 \varepsilon_p^2 V^2}{\left(s_p + \varepsilon_p s_v\right)^2}. \tag{4.1}$$

At $V = 6$ kV, $\Delta s_{\text{Maxwell}} \approx 1.1$ μm, which corresponds to a strain of 1.4 %. Hence, the sample thickness does not significantly change during poling.

CHAPTER V

CONCLUSION AND FUTURE WORK

5.1 Conclusion

The piezoelectric coefficient of charged cellular PP can be optimized by charging in dry nitrogen at elevated pressure. For the material considered in this study, the pressure-dependence of d_{33} is dominated by the charging behavior of voids with heights between 6 and 14 μm. As the pressure is increased from atmosphere pressure, the breakdown field in these voids decreases, allowing more voids to be charged and to contribute to the piezoelectric activity. At pressures above the optimal value of 186 kPa, however, the breakdown field of the larger voids begins to increase, thus reducing the deposited charge density. The modeled d_{33} coefficients are in very good agreement with experimental data, provided that the history of previous charging cycles is taken into account.

5.2 Future Work

Since the Paschen parameters must be modified in order to obtain a good fit between the model and experimental data it is critically important to determine the actual breakdown fields for the micrometer-sized voids that dominate the behavior of the PP material used for this study. Additionally, the box-shaped void approximation used in the model does not account for the height variation within a single void and the possibility that charging may not occur near the edges of each the voids where the void height is small. Refinement of the model using techiques such as the finite-element method could be employed to take these factors into account.

REFERENCES

[1] R. Gerhard-Multhaupt, *Less can be - More holes in polymers lead to a new paradigm of piezoelectric materials for electret transducers*. IEEE Transactions on Dielectrics and Electrical Insulation 9, 850–859 (2002).

[2] S. Bauer, R. Gerhard-Multhaupt and G. Sessler, *Ferroelectrets: Soft electroactive foams for transducers*. Physics Today 57, 37–43 (2004).

[3] X. Zhang, J. Hillenbrand and G. Sessler, *Piezoelectric d(33) coefficient of cellular polypropylene subjected to expansion by pressure treatment*. Applied Physics Letters 85, 1226–1228 (2004).

[4] X. Qiu, *Patterned piezo-, pyro-, and ferroelectricity of poled polymer electrets*. Journal of Applied Physics 108, 011101 (2010).

[5] A. Mellinger, M. Wegener, W. Wirges and R. Gerhard-Multhaupt, *Thermally stable dynamic piezoelectricity in sandwich films of porous and nonporous amorphous fluoropolymer*. Applied Physics Letters 79, 1852–1854 (2001).

[6] X. Zhang, X. Wang, J. Huang and Z. Xia, *Quasi-static and dynamic piezoelectric d (33) coefficients of irradiation cross-linked polypropylene ferroelectrets*. Journal of Materials Science 44, 2459–2465 (2009).

[7] O. Voronina, M. Wegener, W. Wirges, R. Gerhard, L. Zirkel and H. Muenstedt, *Physical foaming of fluorinated ethylene-propylene (FEP) copolymers in supercritical carbon dioxide: single-film fluoropolymer piezoelectrets*. Applied Physics A-Materials Science & Processing 90, 615–618 (2008).

[8] P. Fang, X. Qiu, W. Wirges, R. Gerhard and L. Zirkel, *Polyethylene-naphthalate (PEN) Ferroelectrets: Cellular Structure, Piezoelectricity and Thermal Stability*. IEEE Transactions on Dielectrics and Electrical Insulation 17, 1079–1087 (2010).

[9] S. Zhukov and H. Von Seggern, *Polarization hysteresis and piezoelectricity in open-porous fluoropolymer sandwiches*. Journal of Applied Physics 102, 044109 (2007).

[10] R. A. Pisani Altafim, X. Qiu, W. Wirges, R. Gerhard, R. A. Correa Altafim, H. C. Basso, W. Jenninger and J. Wagner, *Template-based fluoroethylenepropylene piezoelectrets with tubular channels for transducer applications*. Journal of Applied Physics 106, 014106 (2009).

[11] X. Zhang, G. Cao, Z. Sun and Z. Xia, *Fabrication of fluoropolymer piezoelectrets by using rigid template: Structure and thermal stability*. Journal of Applied Physics 108, 064113 (2010).

[12] J. Tang, Y. Duan and W. Zhao, *Characterization and mechanism studies of dielectric barrier discharges generated at atmospheric pressure*. Applied Physics Letters 96, 191503 (2010).

[13] G. Sessler and J. Hillenbrand, *Electromechanical response of cellular electret films*. Applied Physics Letters 75, 3405–3407 (1999).

[14] J. Hillenbrand and G. Sessler, *Piezoelectricity in cellular electret films*. IEEE Transactions on Dielectrics and Electrical Insulation 7, 537–542 (2000).

[15] M. Paajanen, H. Valimaki and J. Lekkala, *Modelling the sensor and actuator operations of the ElectroMechanical Film EMFi*. In: A. Konsta, A. Vassilikou-Dova and K. Vartzeli-Nikaki (eds.), *10th International Symposium on Electrets (ISE 10). Proceedings (Cat. No.99 CH36256)*, pp. 735–8, IEEE Dielectr; Electr. Insulation Soc, IEEE, Piscataway, NJ, USA, 10th International Symposium on Electrets (ISE 10) Proceedings, 22-24 Sept. 1999, Athens, Greece.

[16] M. Paajanen, J. Lekkala and H. Valimaki, *Electromechanical modeling and properties of the electret film EMFI*. IEEE Transactions on Dielectrics and Electrical Insulation 8, 629–636, 10th International Symposium on Electrets, DELPHI, GREECE, SEP 22-24, 1999 (2001).

[17] X. Qiu, A. Mellinger, M. Wegener, W. Wirges and R. Gerhard, *Barrier discharges in cellular polypropylene ferroelectrets: How do they influence the electromechanical properties?*. Journal of Applied Physics 101, 104112 (2007).

[18] S. Zhukov, S. Fedosov and H. von Seggern, *Piezoelectrets from sandwiched porous polytetrafluoroethylene (ePTFE) films: influence of porosity and geometry on charging properties*. Journal of Physics D-Applied Physics 44, 105501 (2011).

[19] P. Zhang, Z. Xia, X. Qiu, F. Wang and X. Wu, *Influence of charging parameters on piezoelectricity for cellular PP film electrets* pp. 39–42, Proc. 12th International Symposium on Electrets, Salvador, Brazil, 11-14 September 2005, IEEE Service Center, Piscataway, NJ (2005).

[20] A. Mellinger and O. Mellinger, *Breakdown Threshold of Dielectric Barrier Discharges in Ferroelectrets: Where Paschen's Law Fails*. IEEE Transactions on Dielectrics and Electrical Insulation 18, 43–48 (2011).

[21] E. M. Bazelyan and Y. P. Raizer, *Spark Discharge*. CRC, Boca Raton, FL (1998).

[22] M. Paajanen, H. Minkkinen and J. Raukola, *Gas diffusion expansion-increased thickness and enhanced electromechanical response of cellular polymer electret films*. In: R. Fleming (ed.), *11th International Symposium on Electrets (ISE11). Proceedings (Cat. No.02CH37383)*, pp. 191–4, IEEE Dielectrics & Electrical Insulation Soc.; IEEE Ultrasonics & Frequency Control Soc, IEEE, Piscataway, NJ, USA, 2002 IEEE International Symposium on Electrets (ISE 11), 1-3 Oct. 2002, Melbourne, Vic., Australia.

[23] M. Wegener, W. Wirges, J. Fohlmeister, B. Tiersch and R. Gerhard-Multhaupt, *Two-step inflation of cellular polypropylene films: void-thickness increase and enhanced electromechanical properties.* Journal of Physics D-Applied Physics 37, 623–627 (2004).

[24] Yongping Wan, Longtao Xie, Xiaoqing Zhang and Zheng Zhong, *Time dependence of piezoelectric d_{33} coefficient of cellular ferroelectret polypropylene film.* Applied Physics Letters p. 122902 (3 pp.) (2011).

[25] K. Kozlov, H. Wagner, R. Brandenburg and P. Michel, *Spatio-temporally resolved spectroscopic diagnostics of the barrier discharge in air at atmospheric pressure.* Journal of Physics D-Applied Physics 34, 3164–3176 (2001).

[26] A. Mellinger, *Dielectric resonance spectroscopy: a versatile tool in the quest for better piezoelectric polymers.* IEEE Transactions on Dielectrics and Electrical Insulation 10, 842–861 (2003).

[27] G. Neugschwandtner, R. Schwodiauer, M. Vieytes, S. Bauer-Gogonea, S. Bauer, J. Hillenbrand, R. Kressmann, G. Sessler, M. Paajanen and J. Lekkala, *Large and broadband piezoelectricity in smart polymer-foam space-charge electrets.* Applied Physics Letters 77, 3827–3829 (2000).

[28] S. Bauer-Gogonea, F. Camacho-Gonzalez, R. Schwoediauer, B. Ploss and S. Bauer, *Nonlinear capacitance dilatometry for investigating elastic and electromechanical properties of ferroelectrets.* Applied Physics Letters 91, 122901 (2007).

[29] X. Qiu, A. Mellinger and R. Gerhard, *Influence of gas pressure in the voids during charging on the piezoelectricity of ferroelectrets.* Applied Physics Letters 92, 052901 (2008).

[30] S. Harris, O. Mellinger and A. Mellinger, *The breakdown threshold of dielectric barrier discharges in piezoelectric polymer foams.* In: *2010 IEEE Conference on Electrical Insulation and Dielectric Phenomena (CEIDP 2010)*, p. 4 pp., IEEE, Piscataway, NJ, USA, 2010 IEEE Conference on Electrical Insulation and Dielectric Phenomena (CEIDP 2010), 17-20 Oct. 2010, West Lafayette, IN, USA.